

NO-A083 574

SRI INTERNATIONAL MENLO PARK CA
FURTHER DEVELOPMENT OF A COMPUTATIONAL SHEAR BAND MODEL.(U)
MAR 80 D C ERICH, D R CURRAN, L SEAMAN

F/8 11/6

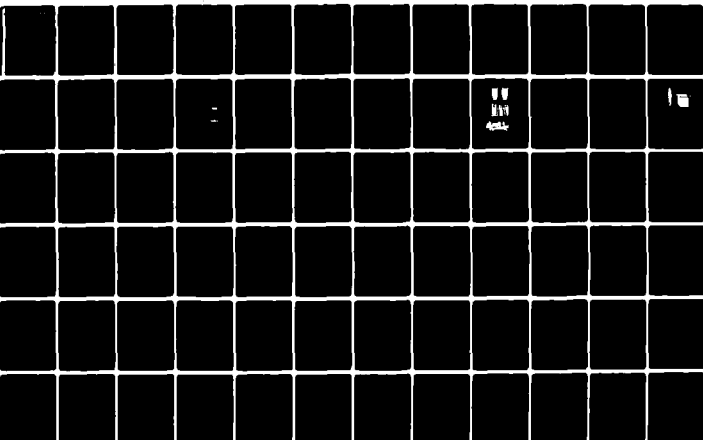
DAA646-77-C-0043

AMMRC-TR-80-3

NL

UNCLASSIFIED

TOP
ALL
180-10



END
DATE
FILED
5-80
DTIC

ADA083574



(12)

LEVEL II

AD

AMMRC TR 80-3

FURTHER DEVELOPMENT OF A COMPUTATIONAL SHEAR BAND MODEL

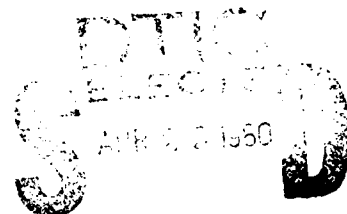
MARCH 1980

D. C. ERLICH, D. R. CURRAN, and L. SEAMAN

SRI International
333 Ravenswood Avenue
Menlo Park, California 94025

Final Report Contract Number DAAG46-77-C-0043

Approved for public release; distribution unlimited.



A

Prepared for

ARMY MATERIALS AND MECHANICS RESEARCH CENTER
Watertown, Massachusetts 02172

80 4 21 071

The findings in this report are not to be construed as an official Department of the Army position, unless so designated by other authorized documents.

Mention of any trade names or manufacturers in this report shall not be construed as advertising nor as an official indorsement or approval of such products or companies by the United States Government.

DISPOSITION INSTRUCTIONS

Destroy this report when it is no longer needed.
Do not return it to the originator.

UNCLASSIFIED

SECURITY CLASSIFICATION OF THIS PAGE (When Data Entered)

REPORT DOCUMENTATION PAGE		READ INSTRUCTIONS BEFORE COMPLETING FORM
1. REPORT NUMBER AMMRC TR-80-3	2. GOVT ACCESSION NO. AD-A083 574	3. RECIPIENT'S CATALOG NUMBER
4. TITLE (and Subtitle) FURTHER DEVELOPMENT OF A COMPUTATIONAL SHEAR BAND MODEL		5. TYPE OF REPORT & PERIOD COVERED FINAL REPORT May 77 - September 1978
7. AUTHOR(s) D. C. Erlich, D. R. Curran, and L. Seaman		6. PERFORMING ORG. REPORT NUMBER PYU-6408
9. PERFORMING ORGANIZATION NAME AND ADDRESS SRI International 333 Ravenswood Avenue Menlo Park, California 94025		8. CONTRACT OR GRANT NUMBER(s) DAAG46-77-C-0043
11. CONTROLLING OFFICE NAME AND ADDRESS Army Materials and Mechanics Research Center Watertown, Massachusetts 02172		10. PROGRAM ELEMENT, PROJECT, TASK AREA & WORK UNIT NUMBERS D/A Project: 1L16205AH84 AMCMS Code: AMCMS Agency Accession:
14. MONITORING AGENCY NAME & ADDRESS (if different from Controlling Office)		12. REPORT DATE March 1980
		13. NUMBER OF PAGES 84
		15. SECURITY CLASS. (of this report) Unclassified
16. DISTRIBUTION STATEMENT (of this Report) Approved for public release; distribution unlimited.		15a. DECLASSIFICATION/DOWNGRADING SCHEDULE
17. DISTRIBUTION STATEMENT (of the abstract entered in Block 20, if different from Report)		
18. SUPPLEMENTARY NOTES		
19. KEY WORDS (Continue on reverse side if necessary and identify by block number) Shear banding Dynamic experiments Fragmenting rounds Constitutive relations Material properties Wave propagation		
20. ABSTRACT (Continue on reverse side if necessary and identify by block number) Experimental and analytical work was performed to improve the previously developed SRI computational model for adiabatic shear band nucleation and growth (SNAG). A series of "contained" fragmenting cylinder experiments were performed with 4340 steel treated to hardness of R 40, R 52, and R 21. The resulting damage ranged from homogeneous plastic deformation to extensive shear banding and resulting fragmentation. The results showed strong positive correlation between shear banding damage		

DD FORM 1 JAN 73 1473 EDITION OF 1 NOV 65 IS OBSOLETE

UNCLASSIFIED

SECURITY CLASSIFICATION OF THIS PAGE (When Data Entered)

UNCLASSIFIED

SECURITY CLASSIFICATION OF THIS PAGE(When Data Entered)

Block No. 20

ABSTRACT

and material hardness for identical loading conditions. A simplified method of damage quantification was used to obtain shear band density, size and orientation distributions for all of the R 40 experiments.

Preliminary computer simulations were performed to determine plastic shear strain rate histories in the direction of the predominant shear banding orientation mode, and the computations were compared with experimental data to yield first estimates for the values of the nucleation and growth parameters.

A shear band nucleation criterion based on measurable material properties was proposed and tested against the experimental data; the criterion was seen to be promising although not yet conclusive.

Several experimental techniques for characterizing the shear banding resistance of materials were evaluated and compared. The contained fragmenting cylinder experiment was concluded to be the best single technique, although the dynamic punch test has special value for armor penetration applications.

UNCLASSIFIED

SECURITY CLASSIFICATION OF THIS PAGE(When Data Entered)

ACKNOWLEDGMENTS

The authors wish to express their appreciation toward Bonita Lew, for performing the computer runs; Albert Rehbock, for setting up and firing the contained fragmenting cylinder experiments; Dante Petro and Margaret Menting, for metallographic analysis; and to the project monitor, John Mescall of U.S. Army Materials and Mechanics Research Center, for helpful discussions.

1

CONTENTS

ACKNOWLEDGEMENTS	1
LIST OF ILLUSTRATIONS	4
LIST OF TABLES	6
1. SUMMARY	7
2. BACKGROUND AND APPROACH	9
3. CONTAINED FRAGMENTING CYLINDER EXPERIMENTS	14
Experimental Technique	14
Qualitative Results	19
Quantitative Results	24
4. COMPUTATIONAL ANALYSIS	33
5. SHEAR BAND NUCLEATION THRESHOLD CRITERION	51
Introduction	51
Background	51
Postulated Nucleation Criterion	53
Relation of Material Properties to	
Flow Field Velocities	54
Examination of Flow Field for Wave Trapping	57
Application of the Criterion to Steel	62
Comparison with Experimental Data	66
Discussion of Postulated Initiation Criterion	70
6. SIMPLIFIED TESTS TO OBTAIN SHEAR BANDING DATA	71
7. DISCUSSION AND RECOMMENDATIONS	74
REFERENCES	77
DISTRIBUTION LIST	79

ILLUSTRATIONS

1. Cross Section of Contained Fragmenting Cylinder Experiments .	15
2. Contained Fragmenting Cylinder Experiments Graphed by Initial Loading Parameters	18
3. 4340 Steel Tubes Recovered from Three Contained Fragmenting Cylinder Experiments Having Identical Loading Parameters but Using Specimen Materials of Different Hardnesses	20
4. Geometry and Nomenclature for Shear Bands in Fragmenting Cylinder Experiments	22
5. Fragment (a) and (b) Used in Shear Band Profile Study, and Measured Profile of Shear Band No. 6 (c)	23
6. Fragment (a) Recovered from Shot 5, and Photomicrographs of Two Zones for Use in Quantitative Shear Band Study (b and c)	25
7. Shear Band Distribution for Shot 2	26
8. Shear Band Distribution for Shot 3	27
9. Shear Band Distribution for Shot 4	28
10. Shear Band Distribution for Shot 5	29
11. Shear Band Distribution for Shot 7	30
12. Shear Band Distribution for Shot 8	31
13. Detonation Velocity (a) and Chapman-Jouguet Pressure (b) for PETN as a Function of Density, according to Hornig et al. . . .	34
14. Polytropic Gas Constant and Chemical Energy Reduced from Data of Hornig et al. on PETN at Several Densities	36
15. Computed Mid-Axial Mode I Plastic Shear Strain Rate Histories (a) for Shots 3 and 5, Compared with Experimentally Determined Shear Band Density Distributions (b)	37
16. Computed Mid-Axial Mode I Plastic Shear Strain Rate Histories (a) for Shots 2, 4, and 7, Compared with Experimentally Determined Shear Band Density Distributions (b)	38

17.	Computed Mid-Axial Mode 1 Plastic Shear Strain Rate History (a) for Shot 8, Compared with Experimentally Determined Shear Band Density Distribution (b)	39
18.	Computed Mid-Axial Mode 1 Peak Plastic Shear Strain Rate as a Function of Detonation Pressure	41
19.	Shear Band Density Distributions Forced to Obey Viscous Growth Law	42
20.	Cell Layout for Computer Simulation of Contained Fragmenting Cylinder Experiments	44
21.	Calculated Pressure History in the HE Adjacent to the Specimen Tube near the Mid-axial Location	45
22.	Calculated Radial Position (a) and Velocity (b) Histories for Specimen Tube at the Mid-axial Location	46
23.	Calculated Principal Stress Histories in the Specimen Tube at the Mid-axial Location	48
24.	Calculated Equivalent Plastic Strain Histories in the Specimen Tube at the Mid-axial Location	49
25.	Calculated Plastic Shear Strain Histories in the Specimen Tube at the Mid-axial Location	50
26.	Deformation Across a Perturbation in the Shear Strain Field	55
27.	Example of Case Where Plastic Wave Trapping Occurs	59
28.	Path Liners of Constant Displacement for Condition of Localization	60
29.	Critical Load Curve for Dynamic Localization	63
30.	Critical Load Curves for Localization of Dynamic Shear Strain	65
31.	Dynamic Load Paths for Shots 15 and 16	67
32.	Comparison of Load Paths for Shear Banded and Non-Shear Banded Material	69
33.	Schematic of Wingrove's Stepped Projectile Technique	72

TABLES

1. 4340 Steel Contained Fragmenting Cylinder Experimental
Parameters and Qualitative Damage Results 17
2. Material Properties for Several Steels 64

1 SUMMARY

The purpose of this program was to improve the previously developed computational model for adiabatic Shear Band Nucleation And Growth (SNAG). Specifically, the goals were to perform careful experiments to obtain quantitative data for improving the growth law for the shear bands, to derive and test a theory for the threshold conditions for nucleation of shear bands, and to establish optimal experimental procedures for measuring the material properties governing shear band behavior.

In pursuit of these goals, we performed seventeen contained fragmenting cylinder experiments with three hardnesses of 4340 steel. (See Figure 1 and Table 1). Quantitative data for the number, size, and orientation distributions of shear bands for the $R_c 40$ experiments were obtained (See Figures 5 through 12); the harder materials were found to be more susceptible to shear banding. Preliminary correlations of these data with computer computations of the strain and stress histories yielded first estimates of the growth parameters in the SNAG model (Figures 15 through 19). A strong dependence on strain rate is apparent.

A theory for the threshold nucleation conditions for shear bands was derived and tested against experimental data (Figure 32). The theory predicts that the shape of the work hardening curve is the key material property governing resistance to shear banding. The comparison with experimental data suggests that the postulated threshold criterion is promising, but more comparisons are needed to confirm its validity.

Several experimental test procedures for measuring shear band behavior were studied. It was concluded that the contained fragmenting cylinder test used in this program is the best single test procedure for measuring the SNAG parameters. However, for specific applications such as armor penetration, supplementary tests that approximate the geometries of interest are desirable.

The results of the program confirm that future work should continue the quantitative data analysis of the contained fragmenting cylinder experiments, as well as further computational analysis to more clearly define the dependence of the SNAG parameters on key material properties. The resulting understanding of the shear banding process in 4340 steel will allow extrapolation to other materials such as those used for armor and penetrators.

2 BACKGROUND AND APPROACH

Shear banding refers to the development of internal regions of localized, intense plastic strain. It is the governing failure mechanism in many cases of armor penetration by plugging, in the disintegration of long rod penetrators, and in the fragmentation of exploding rounds. In previous work^{1,2} for the Naval Surface Weapons Center, the Ballistics Research Laboratory, and the Defense Advanced Research Projects Agency, SRI International performed experimental and analytical work to develop a computational model to describe and predict in quantitative detail the shear banding process. The resulting model, called SNAG for Shear Nucleation And Growth, was used to make reasonable predictions of the fragmentation behavior of cylinders of Armco iron, HF-1 steel, and an actual HF-1 steel fragmenting projectile.

The overall objectives of the present program have been improve the SNAG model for nucleation, growth, and coalescence of adiabatic shear bands, and to establish optimal procedures for characterizing the shear band behavior of materials. Our previous work showed that the nucleation rate and coalescence process are fairly well modeled once the bands have begun to form; the areas of most uncertainty are the threshold conditions that trigger nucleation, and the equations that describe the shear band growth velocities. The specific objectives of the present program were therefore to:

1. Obtain quantitative experimental data to improve the nucleation and growth equations
2. Derive the threshold conditions for shear band nucleation
3. Establish optimal experimental procedures for measuring the material properties governing shear band behavior.

In the design of fragmenting rounds, the growth and coalescence equations are especially important because they determine the fragment size distributions. Hence, our first specific objective is to obtain quantitative data to improve the growth equation.

The second specific objective involving the nucleation threshold conditions is equally important in view of the catastrophic nature of the adiabatic shear banding process. That is, in armor penetration scenarios the onset of shear banding in a significant portion of the armor is often tantamount to failure of the armor by plugging. Thus, an armor designer must attempt to prevent a specific threat from exceeding the threshold conditions. These threshold conditions are then the governing conditions.

The third specific objective, that of establishing optimal experimental and analytical procedures for measuring the key material properties governing shear band behavior, is important for evaluating and characterizing candidate armor and penetrator materials.

The SNAG shear band model developed previously^{1,2} was based on observations of shear banding stopped at early stages in contained fragmenting cylinder experiments similar to those described in detail in the next section.

The experiments performed on HF-1 high fragmentation steel indicated that shear bands nucleate and grow as a function of the plastic strain and strain rate. Bands usually started at the inner diameter of the round, proceeded outwards at 45 degrees to the radial direction, and stayed approximately semicircular. The shear displacement in a band was proportional to the band length. Small ripples or striations nucleated in HF-1 at 15 percent plastic strain and began to grow at about 30 percent plastic strain.

The computational model constructed to represent the experimental phenomena contains nucleation and growth of shear bands, plus a damage-caused stress reduction process. Nucleation occurs according to the equation

$$\frac{dN_{\phi\theta}}{dt} = C_n F_n \left(\frac{1}{E_{cr}} \frac{dE^P}{dt} \right)^2 \frac{d\epsilon_{\phi\theta}^{PS}}{dt} \quad (1)$$

where $N_{\phi\theta}$ is the number of shear bands per unit volume on the $\phi\theta$ plane, t is time, C_n is a coefficient with the units of time squared, F_n is a factor representing the fraction of solid angle assigned to the $\phi\theta$ direction, E_{cr} is a critical energy, dE^P/dt is the rate of increase of plastic strain energy, and $\epsilon_{\phi\theta}^{PS}$ is the plastic shear strain on the $\phi\theta$ plane. The shear bands are not of uniform size but are nucleated with an exponential size distribution.

Growth occurs by the viscous-type growth model:

$$\frac{dR}{dt} = C_g \frac{d\epsilon^{PS}}{dt} R \quad (2)$$

where C_g is a dimensionless growth coefficient, and R is the nominal radius of a band.

The damage on any plane is taken as proportional to ΣNR^3 on that plane. The stress that can be sustained on a plane is reduced in direct proportion to this damage factor.

At the conclusion of the simulation, each computational cell that has undergone shear banding contains a distribution of sizes of shear bands on one or more planes. These distributions are assembled to produce a fragment size distribution for the cell and for the entire object.

With the shear band model, simulations were made of partially and completely fragmenting cylinders and a military round. The correlation of the measured fragment size distributions with the computed ones was quite good for test conditions that included two sizes of cylinders, two loading rates (confined or free), and two materials (HF-1 steel and Armco iron) with very different yield strengths.

At the conclusion of the previous shear band work, it was recognized that there remained several gaps in our knowledge of shear banding. The threshold conditions of strain rate, strain, and stress for initiating shear bands were not understood. Critical temperatures or energies used as nucleation parameters were simply estimated. A growth process was assumed that would be consistent with the final size distributions of shear bands, but there was no experimental basis for uniquely determining the growth rate. The interaction of the three observed shear band modes was not understood, although it was assumed that together the three modes determine the fragment size and shape. Stress-strain relations for partially shear-banded material were derived on the basis of solid mechanics relations plus reasonable physical assumptions. However, these stress-strain relations should receive independent experimental verification before they can be assumed to represent the actual damage processes.

To attack the above deficiencies in the SNAG model, in the present program we have concentrated on designing, performing, and analyzing experiments that would yield optimal information on shear band initiation and growth. As discussed later in Section 6, contained fragmenting cylinder experiments were chosen as the most efficient means for generating the desired data. A theoretical model of shear band initiation was developed (Section 5); this theory predicts that the shape of the work hardening curve for the material is the governing material property for shear band initiation. Therefore, 4340 steels of differing hardness levels and correspondingly differing work hardening curves were chosen for the experiments.

By varying the explosive density and the experimental configurations, we were able to vary the stress and strain histories experienced by the material elements in the exploding cylinders. Computer calculations of these load histories were compared with observed shear band damage, thus allowing initial estimates to be made of the initiation conditions and the shear band growth velocities.

In the remainder of this report we describe in detail the progress we have made toward the program objectives. Section 3 describes the contained fragmenting cylinder experiments, and presents the reduced data from these experiments. Section 4 discusses the computational simulations of the experiments, and presents our first estimates of the parameters obtained for our shear banding model, and Section 5 discusses our proposed shear band nucleation criterion. Section 6 discuss optimal experimental test configurations for characterizing the shear band behavior of materials, and in Section 7 we discuss the results and present our recommendations for further work.

3 CONTAINED FRAGMENTING CYLINDER EXPERIMENTS

Experimental Technique

To obtain quantitative shear banding data on 4340 steel, we used the contained fragmenting cylinder experimental technique devised under a previous program¹ for study of shear banding failure in cylindrical pipes. This technique enables us to load thick-walled cylindrical tubes at pressures and strain rates high enough to induce shear banding, but to contain the tubes in such a manner as to arrest the shear banding process at a level before full fragmentation occurs. We are then able to examine the material metallographically, observe the shear bands, and relate them to the loading histories.

The experimental geometry is shown in Figure 1. The 4340 steel specimen tube is filled with the high explosive PETN^{*}, pressed in 1.27 cm axial increments to a density between 0.7 and 1.47 gm/cm³. A gap is left between the PETN and the upper and lower axial end of the specimen tube in order to prevent unwanted edge effects from shearing off the end of the tube. Detonation occurs through a PETN cone to produce a relatively planar detonation wave traveling down the tube in the axial direction. The high internal pressures from the PETN deform the tube outward, inducing a state of strain that has a large compressive radial component, a large tensile hoop component, and a negligible axial component (ignoring end effects). We thus have a state of high shear strain.

The specimen tube is surrounded by a series of concentric containment pipes. The relatively thin-walled, soft clear acrylic buffer tube allow the specimen cylinder to expand radially and prevents a sharp high-pressure impact with the main containment tube, which is a very thick-walled mild steel pipe. The outermost lead pipe serves as a momentum

*Pentaerythritol tetranitrate ($C_5H_8O_{12}N_4$).

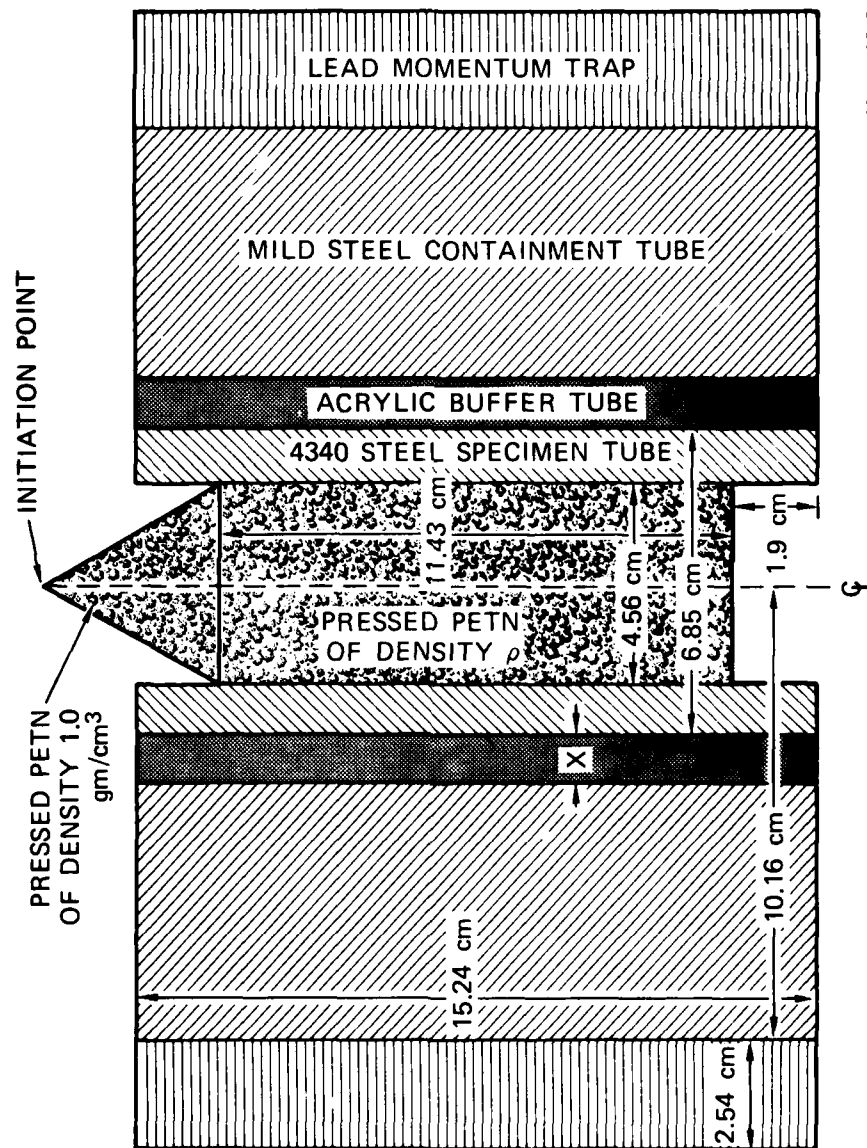


FIGURE 1 CROSS-SECTION OF CONTAINED FRAGMENTING CYLINDER EXPERIMENTS

X varies from 0.64 to 1.9 cm, ρ varies from 0.7 to 1.47 gm/cm³.

trap; it separates from the mild steel pipe and moves out in the radial direction, taking most of the radial momentum with it and reducing the magnitude of the inward-going tensile wave. Because of the thickness of the containment tubes, the specimen tube experiences no radial tensile stress for at least 40 μ sec, by which time the internal pressures produced by the PETN are greatly reduced, due to escape of explosive gases from the open ends of the tube. The lack of radial tensile stresses inhibits brittle fracture, leaving shear banding as the predominant failure mode in the specimen tube.

The strain and strain rate to which the specimen tube is subjected are varied by changing the explosive mixture and the thickness of the acrylic buffer tube. A higher pressure detonation will induce higher strain rates in the specimen tubes, and a thicker buffer will allow the specimen tube to attain larger strains. However, the controlling parameters are not orthogonal with respect to the material response parameters. For example, a higher detonation pressure will produce larger strains even if the buffer tube thickness remains the same. Furthermore, there is a complicated pattern of stress waves and reflections while the various containment tubes are "ringing up" to their peak pressures and then unloading. Hence, the loading history of the specimen tube cannot be predicted easily without the aid of computer simulations. In section 4 we present the results of the computer simulations and show, for example, how the computed strain rates vary with detonation pressure.

A total of seventeen contained fragmenting cylinder experiments were performed in this program, using commercially obtained tubular 4340 steel as the specimen material. Eight shots were fired using the 4340 steel treated to $R_c 40$, seven used steel treated to $R_c 52$, and two used fully annealed steel ($\sim R_c 21$). The experimental parameters for each shot are given in Table 1 and are also depicted graphically in Figure 2, which shows the location of each experiment in PETN density--acrylic buffer thickness space. On this graph, a positive change in the horizontal position would represent a greater shear strain loading rate in the specimen, and a positive vertical change would represent a greater

Table 1

4340 STEEL CONTAINED FRAGMENTING CYLINDER EXPERIMENTAL PARAMETERS
AND QUALITATIVE DAMAGE RESULTS

Shot No.	Specimen Hardness	Acrylic Buffer Thickness (cm)	PETN Explosive Density (g/cm ³)	Calculated Detonation Pressure (kbars)	Qualitative Damage Results	
					Shear Banding	Fragmentation
1	R _C 40	0.95	1.00	80	Incipient	Negligible
2		1.27	1.20	122	Moderate	Negligible
3		1.27	1.35	163	Moderate	Negligible
4		1.59	1.20	122	Moderate	Negligible
5		1.59	1.35	163	Extensive	Moderate
6		0.95	1.20	122	Negligible	Negligible
7		1.90	1.20	122	Extensive	Negligible
8		0.95	1.47	204	Extensive	Extensive
10	R _C 52	1.27	1.35	163	Extensive	Extensive
11		0.95	1.20	122	Moderate	Moderate
12		1.59	1.00	80	Extensive	Extensive
13		0.95	1.00	80	Incipient	Negligible
14		0.64	1.20	122	Negligible	Negligible
15		1.59	0.85	54	Moderate	Moderate
16		1.90	0.70	33	Incipient	Negligible
20		1.27	1.35	163	Incipient	Negligible
21	R _C 21	0.95	1.35	163	Incipient	Negligible
17						

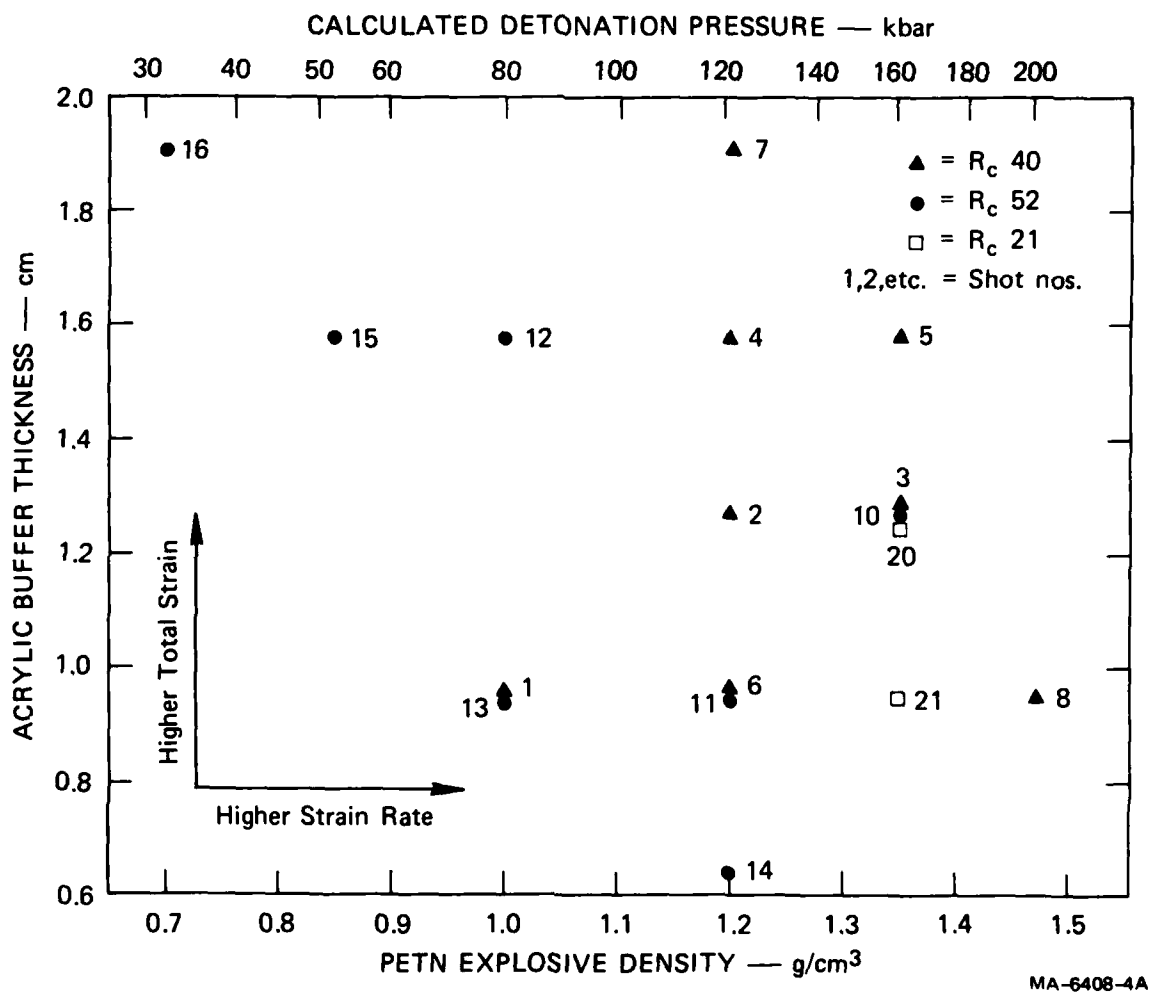


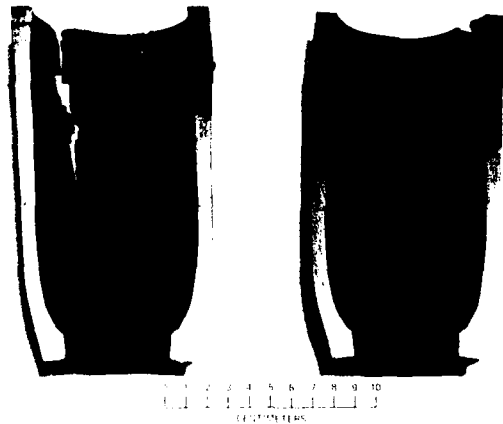
FIGURE 2 CONTAINED FRAGMENTING CYLINDER EXPERIMENTS GRAPHED BY INITIAL LOADING PARAMETERS

loading duration. Either change or a combination of both should lead to a greater level of shear band damage.

The loading parameters for the $R_c 40$ and $R_c 52$ experiments were selected to cover a broad range of damage from negligible shear banding (homogeneous deformation only) to substantial fragmentation. Qualitative damage results are given in Table 1. The experimental series were also designed so that, for several cases, experiments having identical loading parameters would be performed using specimen materials of the different hardnesses, so as to compare the resistance to shear banding as a function of material hardness or yield strength.

Qualitative Results

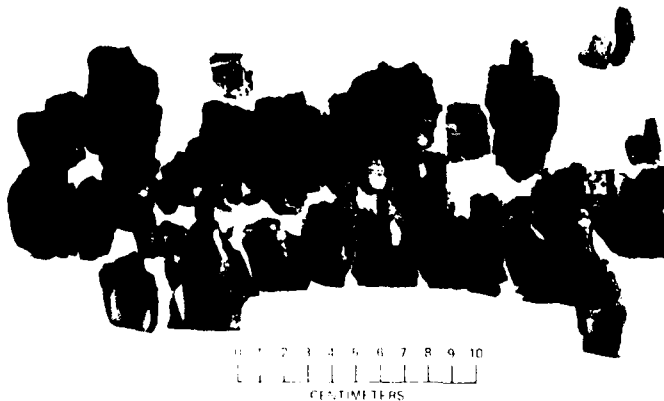
For the shots resulting in less damage, the specimen tube was recovered in one or two large pieces, which we then sliced parallel to the axis to make the inner surface more visually accessible (Figures 3a and 3b). For the shots resulting in more damage, the tube was fragmented into as many as 30 pieces. The recovered fragments were arranged into a jig-saw-puzzle-type pattern according to their relative position in the original specimen tube (e.g., as in Figure 3c), so that we could determine the damage as a function of axial position in the tube. Comparison of the fragments recovered from shots with identical loading parameters, but with specimen materials of different hardness (as in Figure 3), showed that the harder material will shear band more readily. The fully annealed ($R_c 21$) 4340 steel exhibited no shear banding (except for three large shear cracks that originated at or near the upper end of the tube as a result of edge effects altering the basic strain pattern) despite having undergone a very large amount of homogeneous plastic deformation. In contrast, the substantially hardened $R_c 40$ steel exhibited numerous small shear bands widely scattered over most of the inner surface, although it experienced only about half as much homogeneous plastic deformation, and the extremely hardened $R_c 52$ steel exhibited extensive shear banding leading to fragmentation after even less homogeneous plastic deformation. In Section 5, we discuss reasons for this effect.



(a) SHOT 20, R_c21



(b) SHOT 3, R_c40



(c) SHOT 10, R_c52

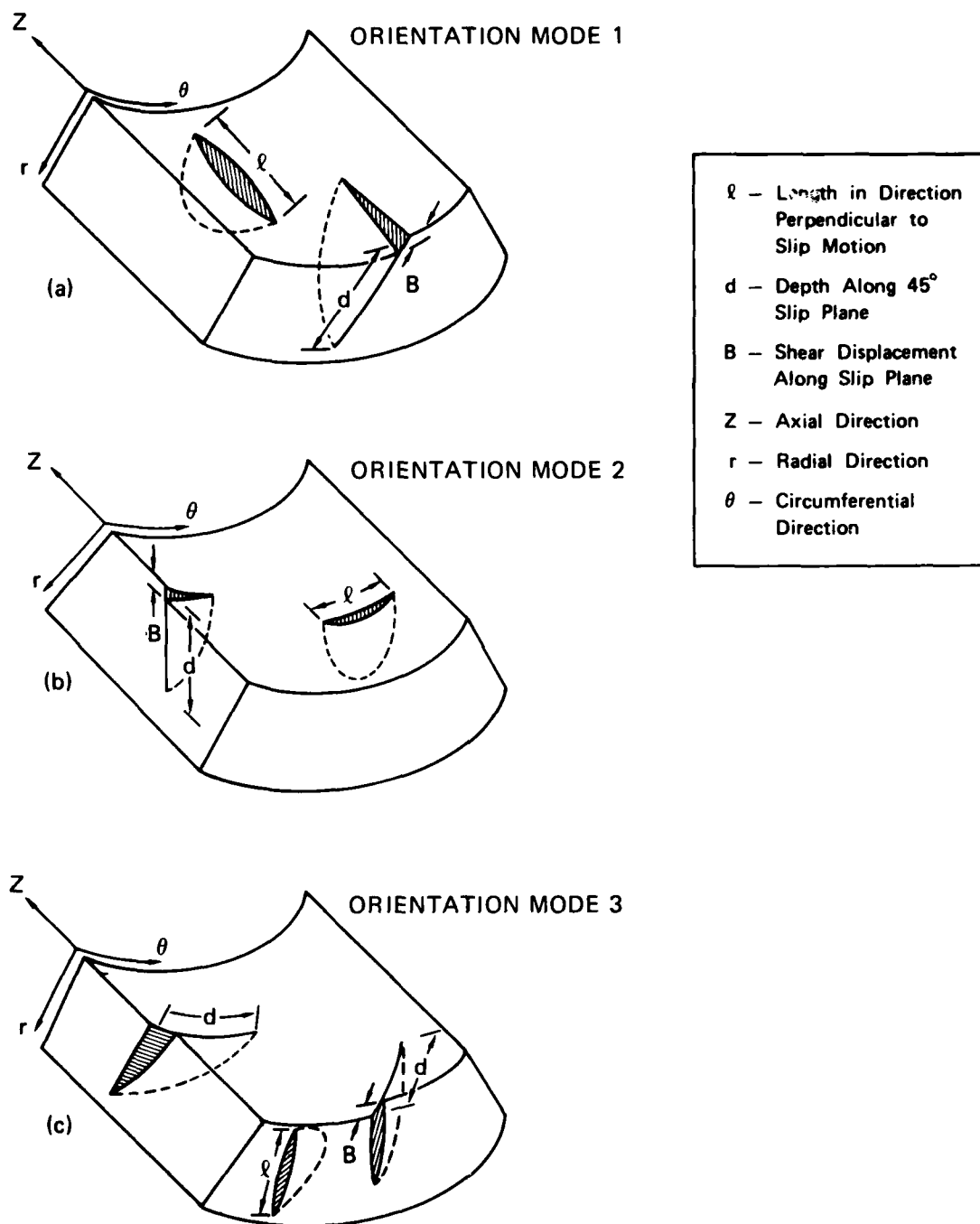
MA-6408-12A

FIGURE 3 4340 STEEL TUBES RECOVERED FROM THREE CONTAINED FRAGMENTING CYLINDER EXPERIMENTS HAVING IDENTICAL LOADING PARAMETERS BUT USING SPECIMEN MATERIALS OF DIFFERENT HARDNESSES

The three orientation modes for shear bands in an expanding cylinder are shown in Figure 4. As discussed in detail by Erlich et al.,¹ the modes represent shear slip along the plane of maximum shear strain. In this present study of 4340 steel, as well as in the previous study of HF-1 steel, the mode 1 shear bands predominate. They are the only ones evident in the experiments producing lower damage levels. At the higher levels of damage, although mode 2 bands appear at the inner surface in significant numbers and mode 3 bands are occasionally seen in the interior, it is still the mode 1 bands that have become the longest and have taken up the most strain. The mode 1 bands extend all the way through a specimen or coalesce with other mode 1 bands to cause fragmentation into axial strips, although the mode 2 bands may determine the length or aspect ratio of these strips.

In the previous shear banding study of HF-1 steel,¹ it was determined that more than two-thirds of the mode 1 shear bands created in a contained fragmenting cylinder experiment intersected the inner surface of the specimen tube. It was also determined that the length (ℓ) of the shear band in the direction perpendicular to its slip plane (see Figure 4) was approximately twice its depth (d) along the slip plane and that the depth was roughly 15 times the maximum shear displacement (B) along the slip plane.

To determine if these findings also hold true for 4340 steel, we selected a fragment from shot 2, shown in Figure 5, and made a series of seven cuts perpendicular to the tube axis with a thin diamond blade. We polished and etched each cut surface, identified the mode 1 shear bands common to adjacent cuts and measured the shear band depth and displacement on each cut. The results for one shear band, labeled no. 6, are given in Figure 5c, which shows d and B plotted against the relative distance along ℓ . The band appears to have a half-length of almost 6-1/2 mm, a maximum depth of about 7-1/2 mm, and a maximum shear displacement of $\sim 2/3$ mm. Its shape is very nearly that of a semicircle; thus, if a band is assumed to nucleate at one point, it grows in depth about as much as it grows in length in each direction. The depth appears to be on the order of 11 or 12 times the displacement. In addition, all



MA-5084-21A

FIGURE 4 GEOMETRY AND NOMENCLATURE FOR SHEAR BANDS IN FRAGMENTING CYLINDER EXPERIMENTS

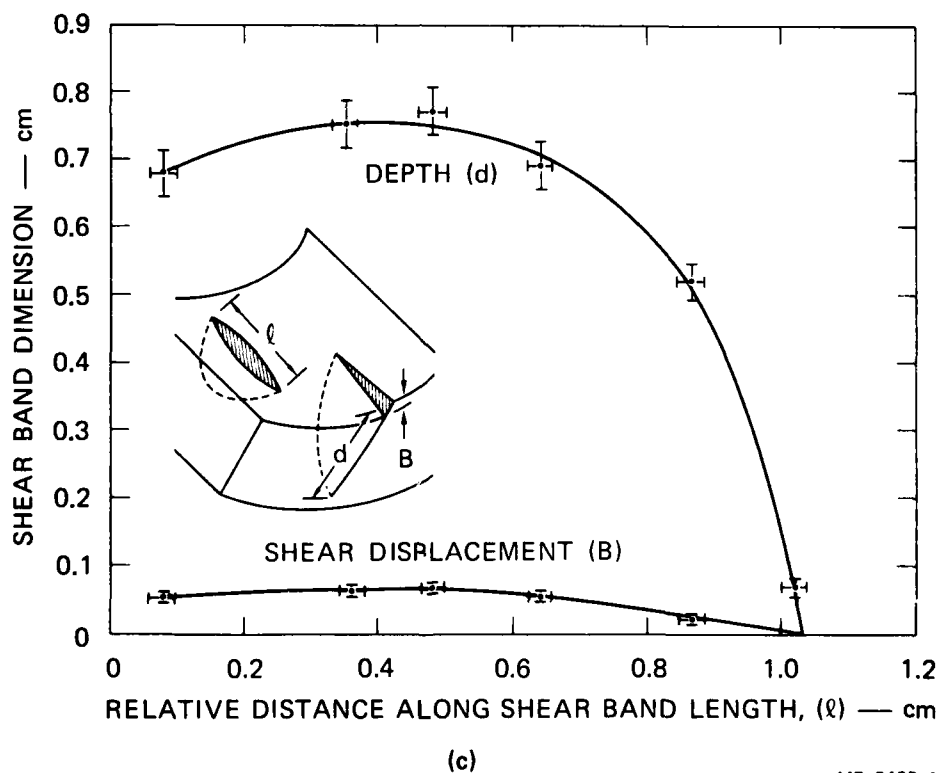
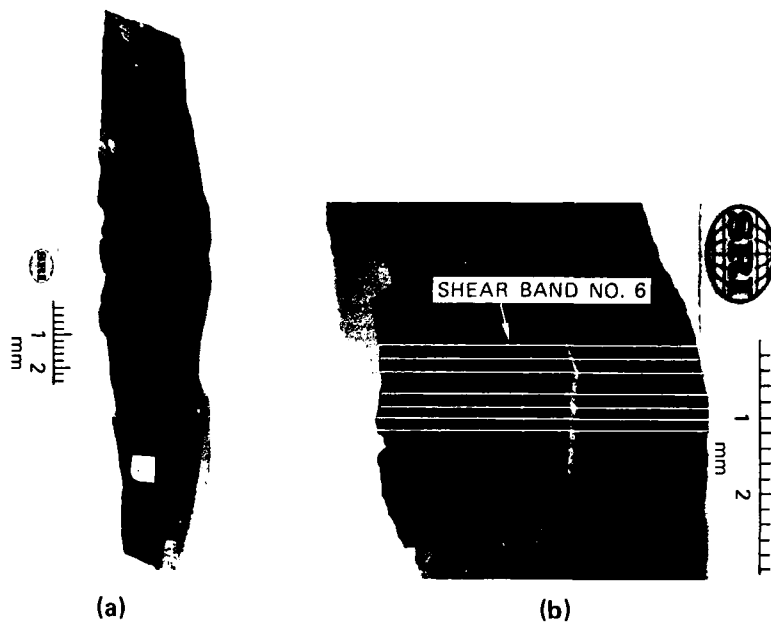


FIGURE 5 FRAGMENT (a) AND (b) USED IN SHEAR BAND PROFILE STUDY, AND MEASURED PROFILE (c) OF SHEAR BAND NO. 6

the mode 1 bands seen on the cuts in this fragment or any other 4340 steel fragment intersected the inner surface of the specimen tube.

It was noticed that for shots resulting in small amounts of shear banding damage, the specimen tube would sometimes separate along a diagonal line that would around the tube at approximately 15° to 20° from the axial direction (as in Figure 3b). For shots with more substantial shear banding damage, often the shear bands would link up along this same diagonal direction, although each individual band was formed parallel to the axis. It is believed that this effect is caused by texturing of the 4340 steel tube in the process of extrusion.

Quantitative Results

As a result of the findings discussed above, we were able to simplify our method for determining quantitative shear band damage. Rather than making a large number of cuts in each fragment and polishing, etching, and photographing the surface of each cut, and then measuring the depth of each shear band, we decided to photograph in detail the inside surface of each fragment and measure the length and axial position of each shear band. This procedure is much less time consuming.

As an example, Figure 6 shows photomicrographs of part of one fragment recovered from Shot 5 that were used in the quantitative shear band determination. Two photomicrographs with side lighting from opposite directions (Figure 6b and 6c) are used to highlight the mode 1 shear bands intersecting the surface at the two orthogonal 45° angles. The fragment is divided into zones of axial position, each zone being 1.27 cm wide, and shear bands within each zone are counted as a function of length. Values for each zone are added together for all of the fragments recovered for a particular lot, and the total is divided by the surface area of the zone to yield shear band surface densities.

Quantitative damage assessments were made only for the shots using 4340 steel specimen tubes hardened to $R_c 40$ (except for Shots 1 and 6, which exhibited negligible shear banding). The results are shown in Figures 7 through 12, plotted in terms of the areal density of shear

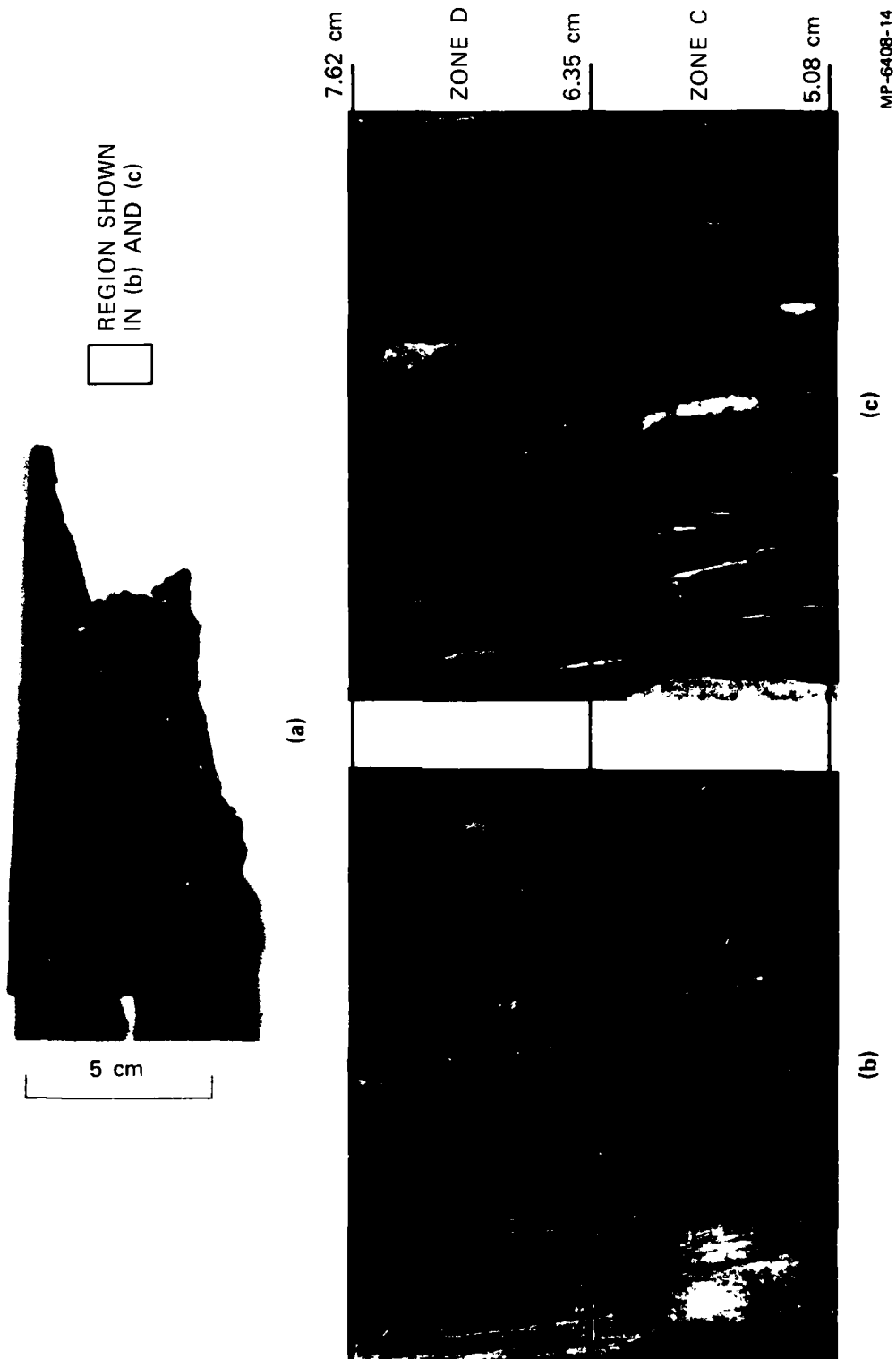


FIGURE 6 FRAGMENT (a) RECOVERED FROM SHOT NO 5, AND PHOTOMICROGRAPHS (b and c) OF TWO ZONES FOR USE IN QUANTITATIVE SHEAR BAND STUDY

Note shading differences between (b) and (c). Distances are from one end of cylinder.

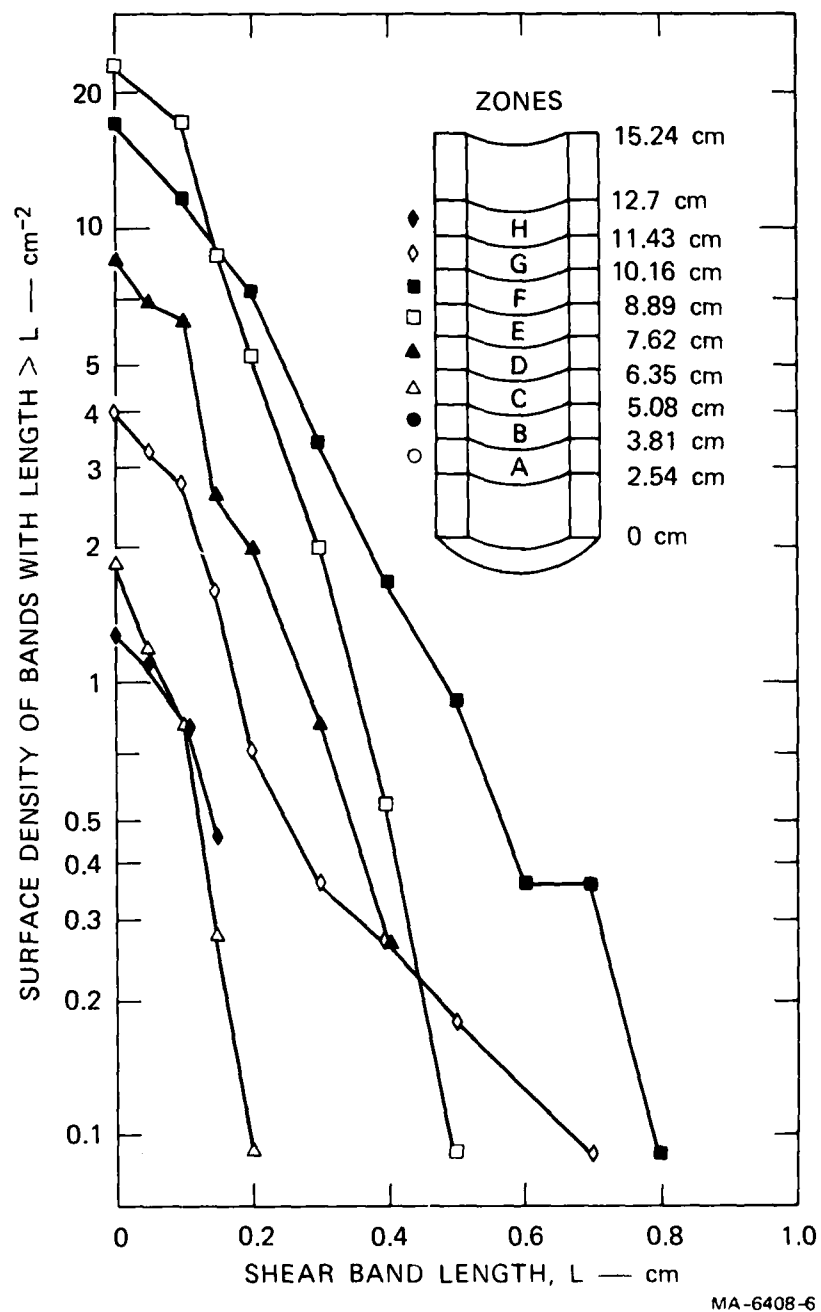
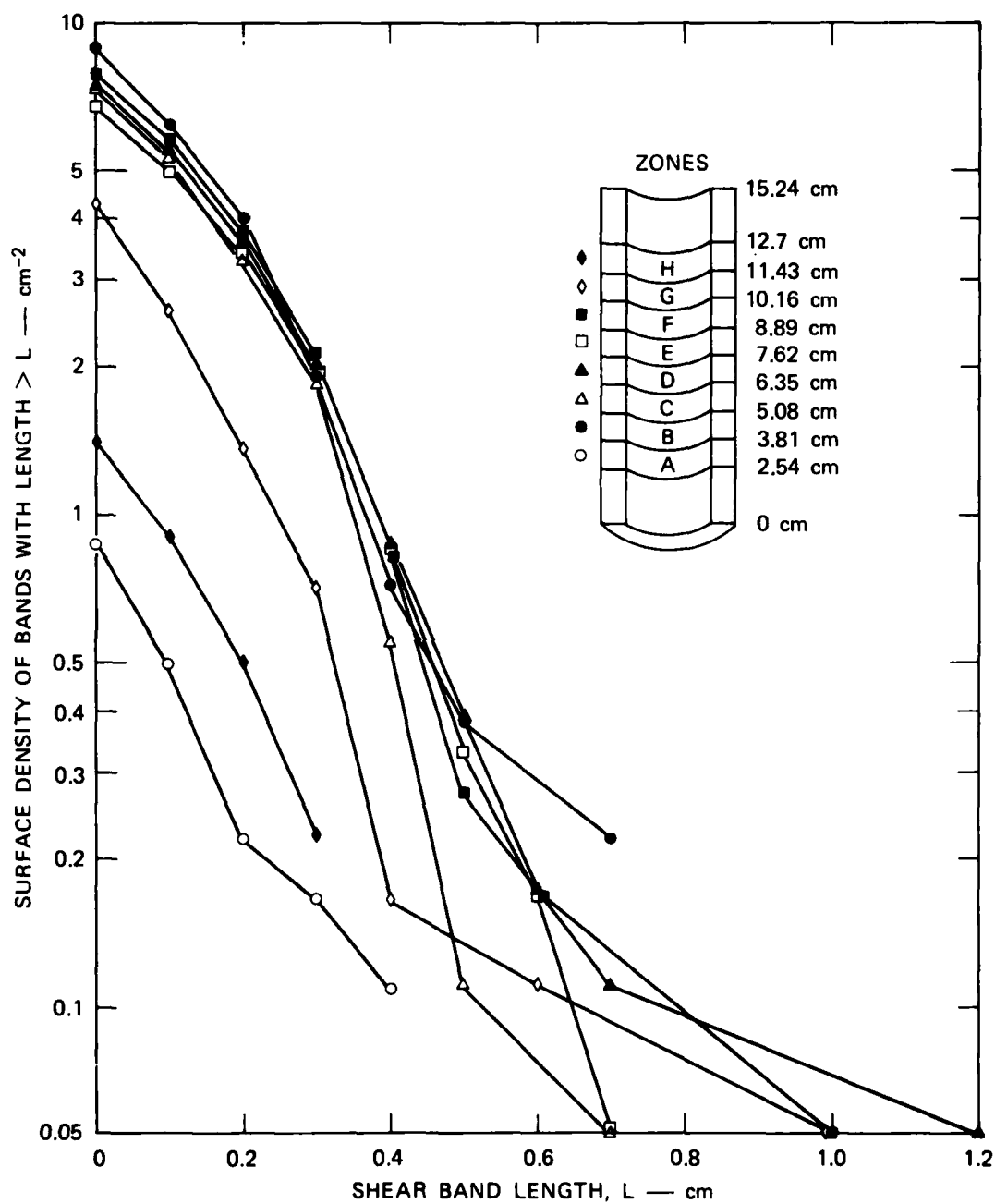


FIGURE 7 SHEAR BAND DISTRIBUTION FOR SHOT 2



MA-6408-8

FIGURE 9 SHEAR BAND DISTRIBUTION FOR SHOT 4

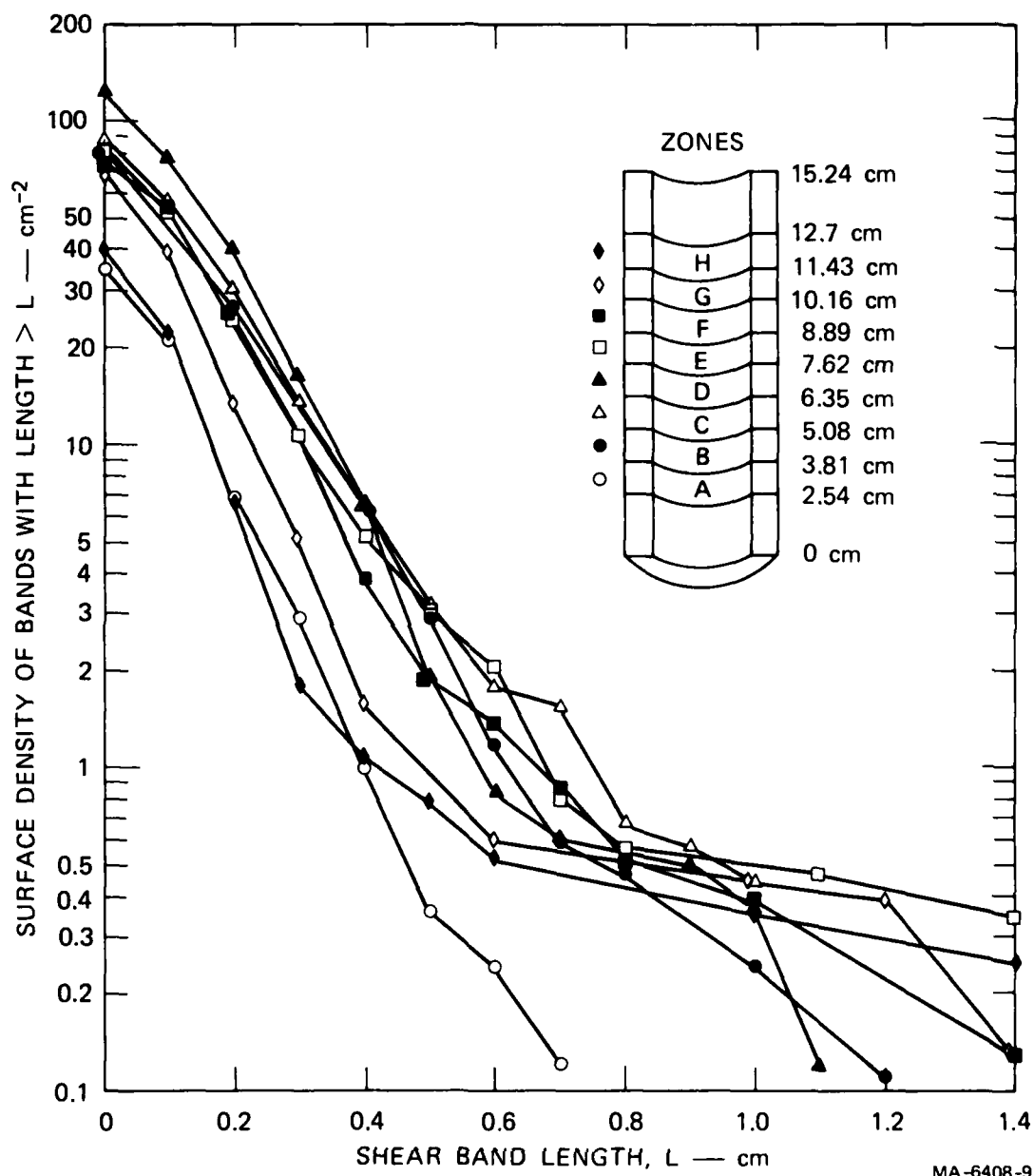
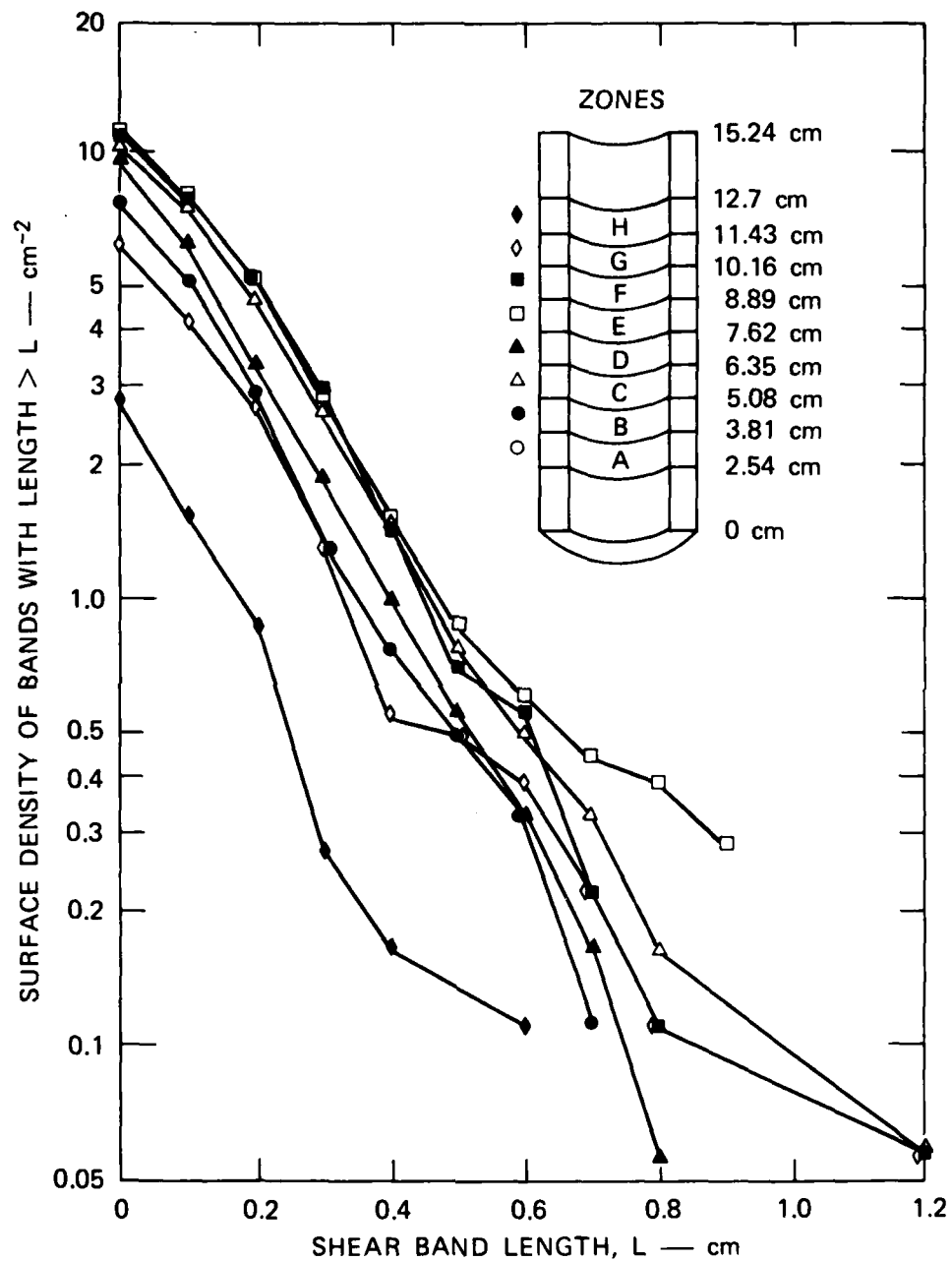
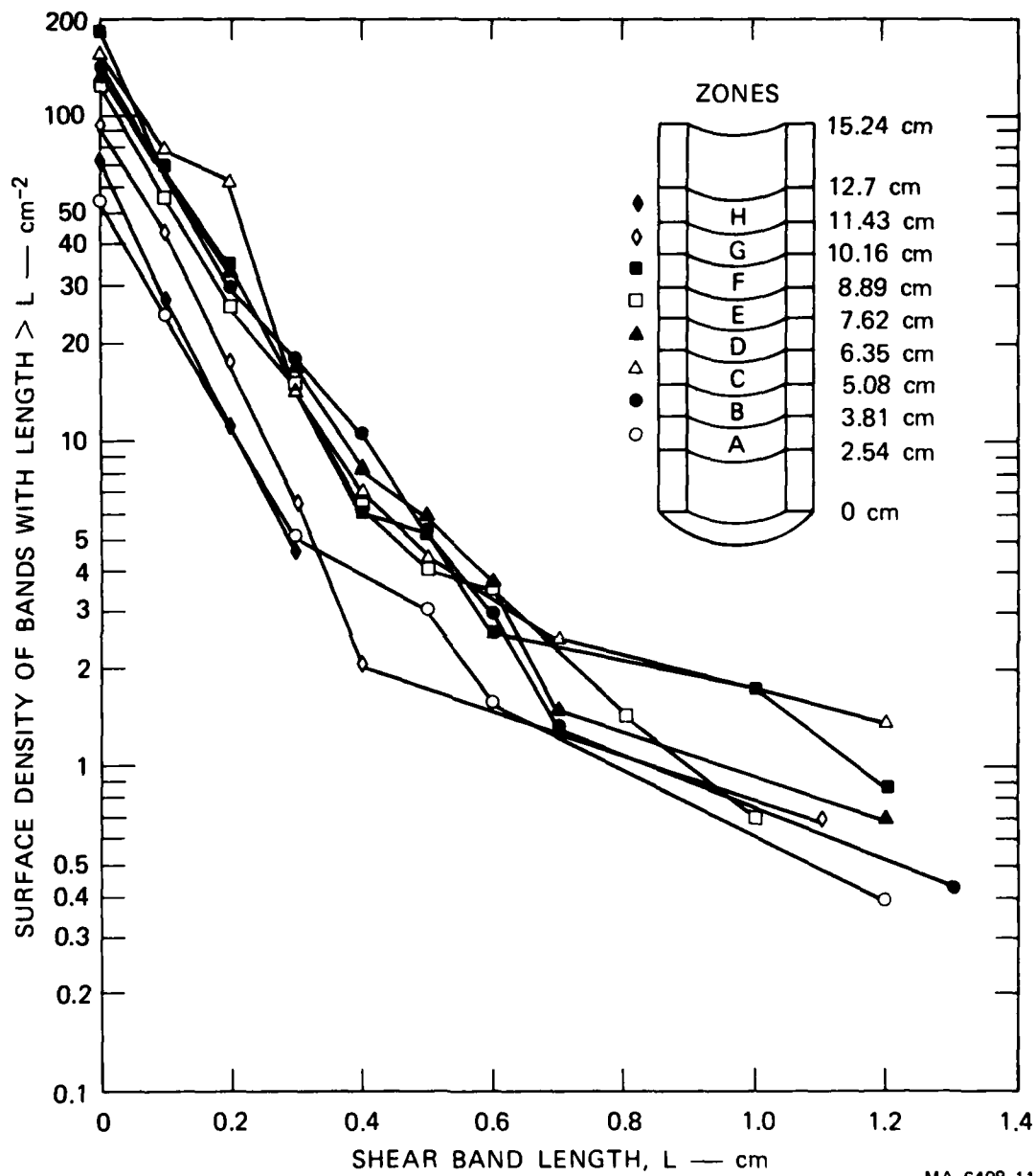


FIGURE 10 SHEAR BAND DISTRIBUTION FOR SHOT 5



MA-6408-10

FIGURE 11 SHEAR BAND DISTRIBUTION FOR SHOT 7



MA-6408-11

FIGURE 12 SHEAR BAND DISTRIBUTION FOR SHOT 8

bands having a length greater than ℓ versus the shear band length ℓ , for different zones of axial position.

In examining the graphs, one should note several features. First, the shear band densities are higher for zones near the axial mid-point of the specimen tube than for zones near either end. This is because the pressures from the explosives remained higher for a longer duration. Second, the very small shear bands having a length less than about 0.2 cm are difficult to see, since the width of their exposed slip plane (B, from Figure 5) may be less than 0.1 mm; hence, the number of these bands counted may be below the actual value. Therefore, the shear band density curves for values of ℓ less than 0.2 cm (see Figure 7, for example) may actually be as steep as they are for larger values of ℓ .

In summary, we have performed a series of contained fragmenting round experiments on specimens of 4340 steel treated to three different hardnesses and have observed a range of damage from homogeneous plastic deformation only to extensive shear banding and fragmentation. We devised a simplified method of quantifying the shear banding damage and obtained shear band density distributions as a function of axial position for each of the $R_c 40$ steel experiments. Quantification of the shear band damage for the $R_c 52$ steel experiments is recommended for future work.

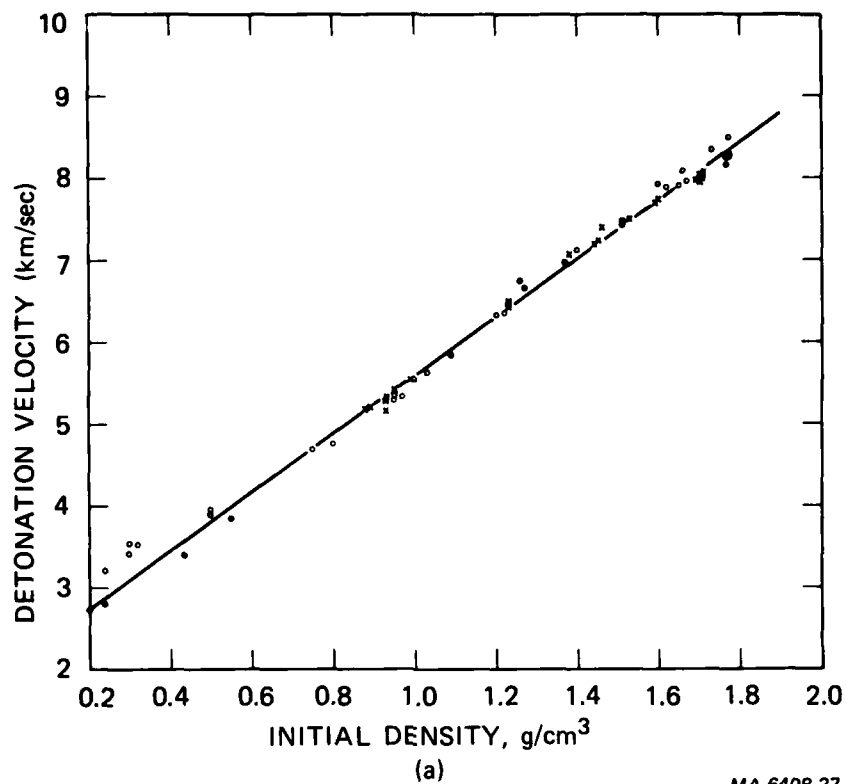
4 COMPUTATIONAL ANALYSIS

The TROTT computer code, which was developed recently at SRI and documented by Seaman,³ was used to simulate all the R_c40 contained fragmenting round experiments for which we had shear band density distributions. The TROTT code is a two-dimensional Lagrangian wave propagation code incorporating most of the complex equations-of-state and fracture models available in the one-dimensional PUFF code⁴. The original calculations with the TROTT code did not utilize a slide line at the HE-specimen tube interface. Therefore, in the simulations the explosive gases are not allowed to escape from the top and bottom of the specimen tube as fast as they would in the actual experiment. However, this was not expected to greatly affect the pressure histories in the mid-axial regions until reasonably late in the simulation (≈ 30 μ sec), so that the response of the specimen tube in the mid-axial zones (zones D & E in Figures 7 through 12) may be approximated fairly well by the TROTT code without the slide line.

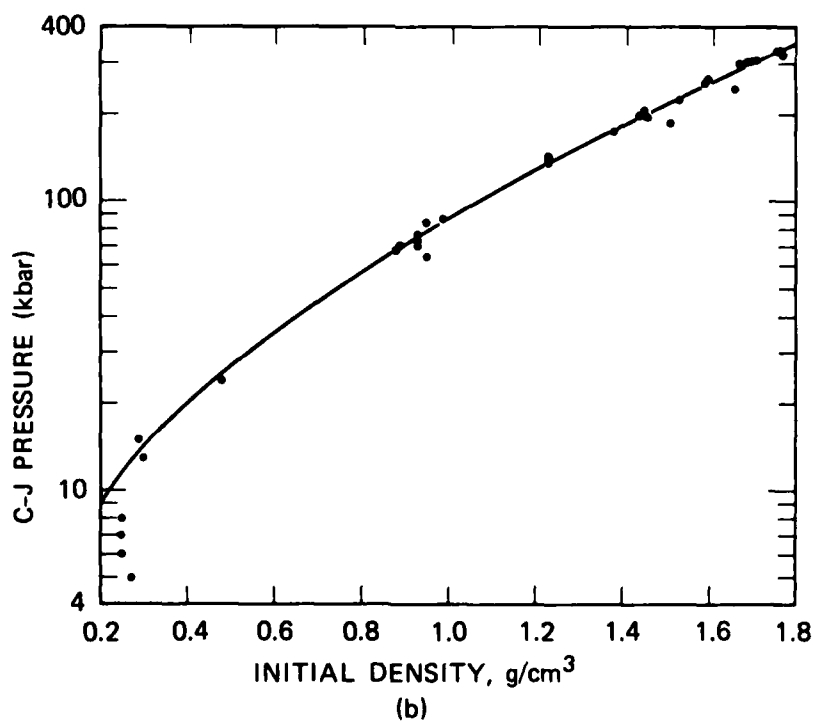
The equation of state for reduced density PETN was obtained from the experimental data of Hornig, Lee, Finger, and Kurrle.⁵ They measured Chapman-Jouguet pressures (peak detonation pressures) and detonation velocities in PETN for densities from 0.25 g/cm³ to 1.764 g/cm³ (approximately the crystal density). For our calculations the data were fitted to a polytropic gas form to obtain the polytropic gas constant γ and the chemical energy Q .

To fit the data to the polytropic form, the detonation velocity D and pressure P_{CJ} were plotted versus density as shown in Figure 13. A smooth curve was drawn through the points. The values of γ and Q were obtained from the polytropic gas relations

$$\gamma = \frac{\rho_o D^2}{P_{CJ}} - 1, \quad \text{and} \quad Q = \frac{P_{CJ}}{2\rho_o(\gamma - 1)}$$



MA-6408-27



MA-6408-28

FIGURE 13 DETONATION VELOCITY (a) AND CHAPMAN-JOUQUET PRESSURE (b) FOR PETN AS A FUNCTION OF DENSITY, ACCORDING TO HORNIG et al.⁵

where D = detonation velocity, cm/sec

P_{CJ} = Chapman-Jouguet pressure, dyn/cm²

Q = chemical energy, erg/g

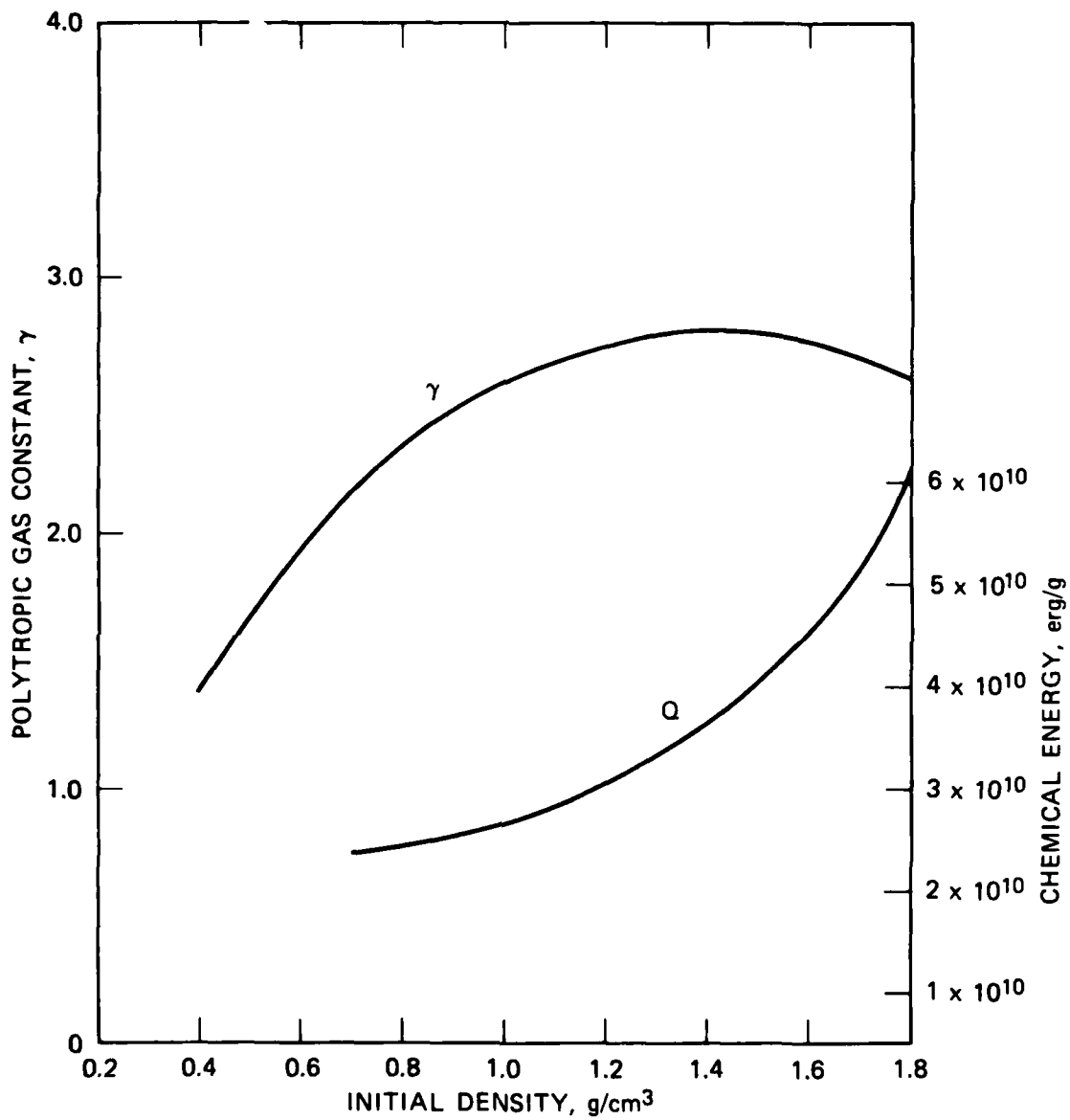
ρ_0 = initial density, g/cm³

The resulting constants for the PETN are shown in Figure 14. These constants were used in our simulations of fragmenting round experiments.

The simulations were made using the shear banding subroutine SHEAR2¹ so as to calculate the plastic shear strain in directions appropriate to each of the three orientation modes for shear banding in a cylindrically expanding pipe. The parameters were set in these calculations so as not to allow any shear bands to nucleate or grow. Thus, the simulations were for the case of negligible shear banding. They would be expected to be accurate for experiments that produced negligible or incipient shear banding or for experiments that produced higher damage levels before the onset of significant band growth, at which time significant strains would be taken up by the shear bands themselves. In any case, the simulations would give a first approximation to the strain histories.

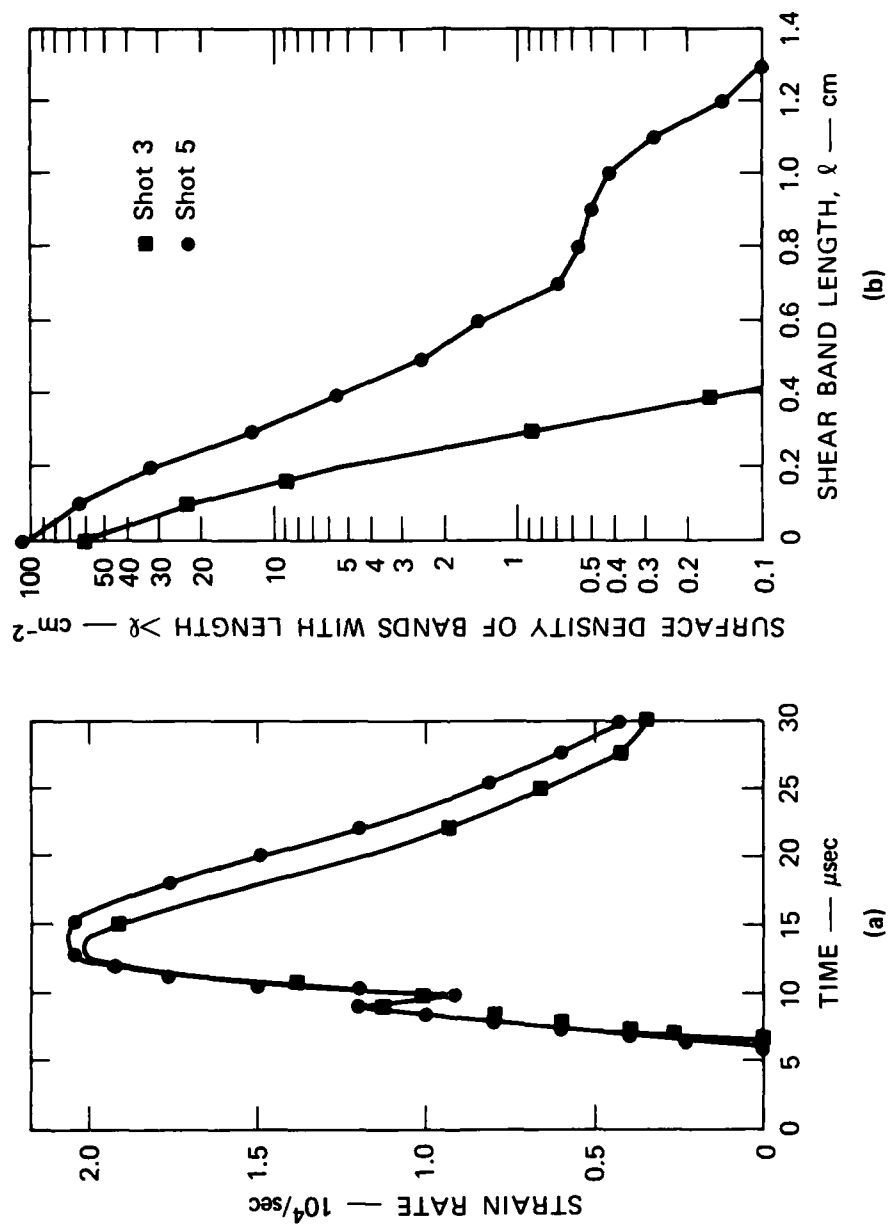
Since the shear band density distributions that we measured quantitatively from the R_C40 experiments involved mode 1 shear bands only, we calculated mode 1 strain histories (Ref. 1, p. 35). The strain rate history was selected because the strain rate is the parameter analogous to the stress in the case of tensile failure. Just as the growth rate of tensile voids and cracks depends on the tensile stress,⁶ we expect that the shear band growth rate depends on the shear strain rate.

The plastic shear strain rate histories and the shear band density distributions for the mid-axial location (an average of zones D & E in Figures 7 through 12) are grouped according to the explosive density in Figures 15 through 17. Figure 15 includes Shots 3 and 5, both of which had an H.E. density of 1.35 g/cm³; Figure 16 includes Shots 2, 4,



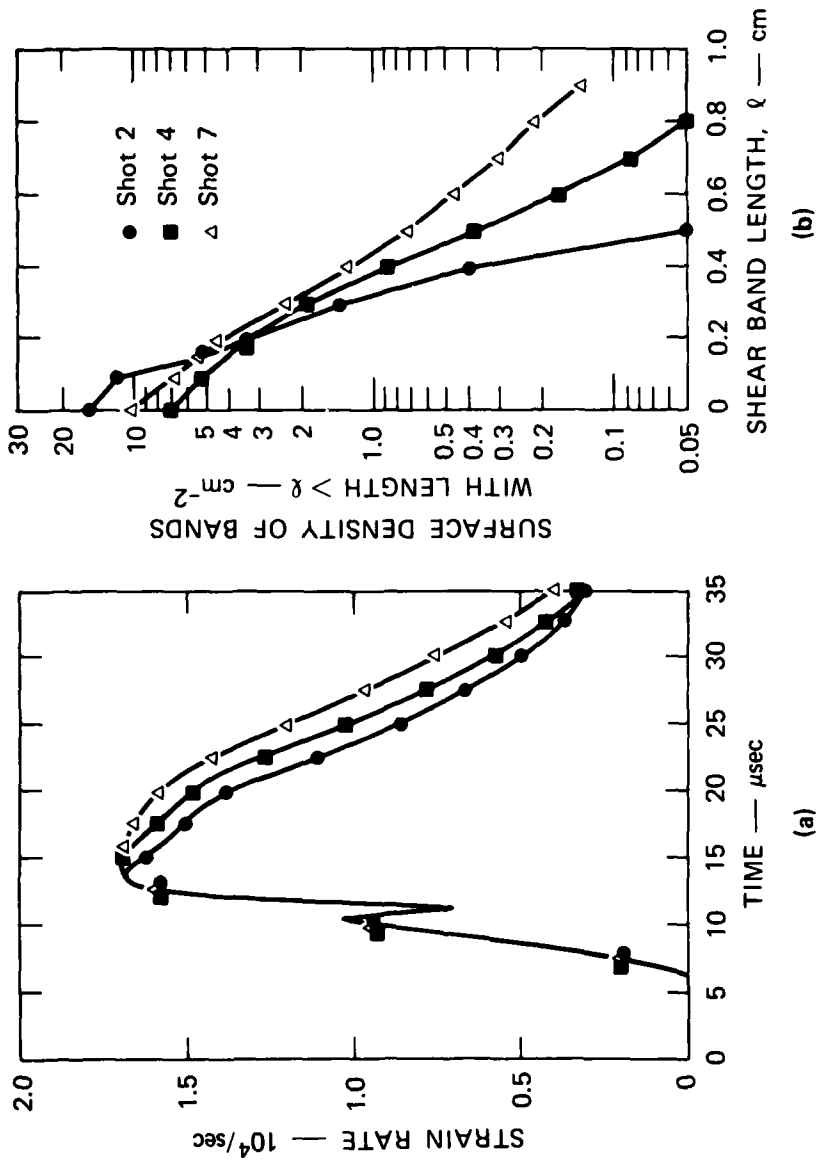
MA-6408-29

FIGURE 14 POLYTROPIC GAS CONSTANT γ AND CHEMICAL ENERGY Q REDUCED FROM DATA OF HORNIG et al.⁵ ON PETN AT SEVERAL DENSITIES



MA-6408-15

FIGURE 15 COMPUTED MID-AXIAL MODE 1 PLASTIC SHEAR STRAIN RATE HISTORIES
(a) FOR SHOTS 3 AND 5, COMPARED WITH EXPERIMENTALLY DETERMINED
SHEAR BAND DENSITY DISTRIBUTIONS (b).



MA-6408-16

FIGURE 16 COMPUTED MID-AXIAL MODE 1 PLASTIC SHEAR STRAIN RATE HISTORIES
(a) FOR SHOTS 2, 4, AND 7, COMPARED WITH EXPERIMENTALLY DETERMINED
SHEAR BAND DENSITY DISTRIBUTIONS (b).

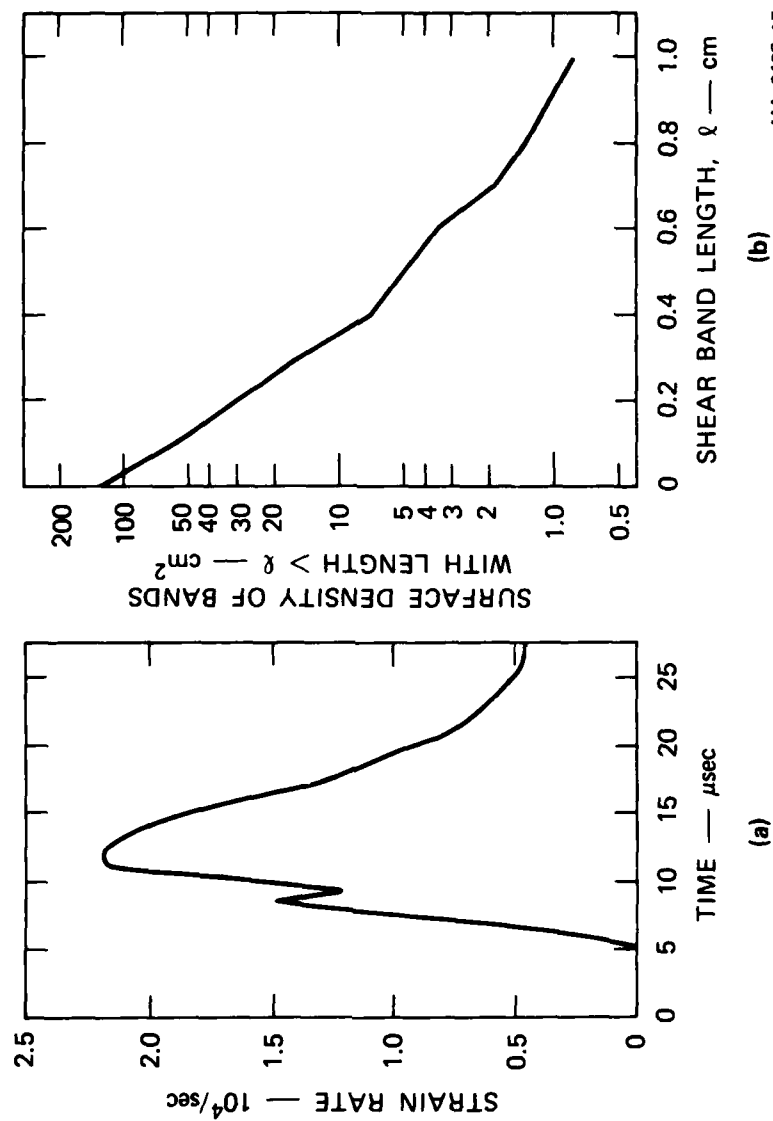


FIGURE 17 COMPUTED MID-AXIAL MODE 1 PLASTIC SHEAR STRAIN RATE HISTORY (a) FOR SHOT 8
 COMPARED WITH EXPERIMENTALLY DETERMINED SHEAR BAND DENSITY DISTRIBUTION (b)

MA-6408-17

and 7, all of which had an H.E. density of 1.2 g/cm^3 ; and Figure 17 depicts Shot 8, which had an H.E. density of 1.47 g/cm^3 .

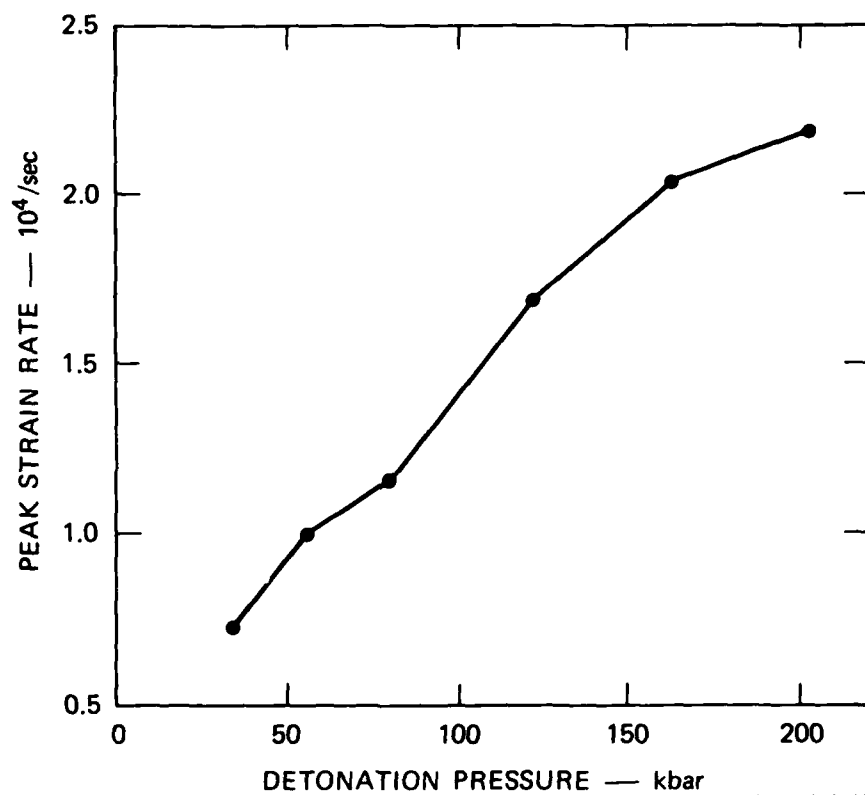
The peak strain rates are almost exactly the same for shots having the same H.E. density and hence the same detonation pressures. These peak strain rates are shown in Figure 18 as a function of detonation pressure. The rates range from $0.7 \times 10^4/\text{sec}$ for a detonation pressure of 33 kbar to $2.2 \times 10^4/\text{sec}$ for a detonation pressure of 204 kbar. For shots of a given H.E. density, increasing the acrylic buffer thickness increases the shear strain rate duration but not the peak amplitude. The change in the computed pulse duration appears to vary linearly with the increase in buffer thickness and, in fact, has a value equal to the time it takes a stress pulse to traverse back and forth across the change in thickness.

From the shear band density distributions and the strain rate histories shown in Figure 15 and 16, it appears that:

- (1) Higher strain rates result in greater shear band nucleation rates.
- (2) A slight increase in the duration of the peak strain rates causes a marked increase in the shear band lengths.
- (3) The shear band growth rates are larger for higher peak strain rates.

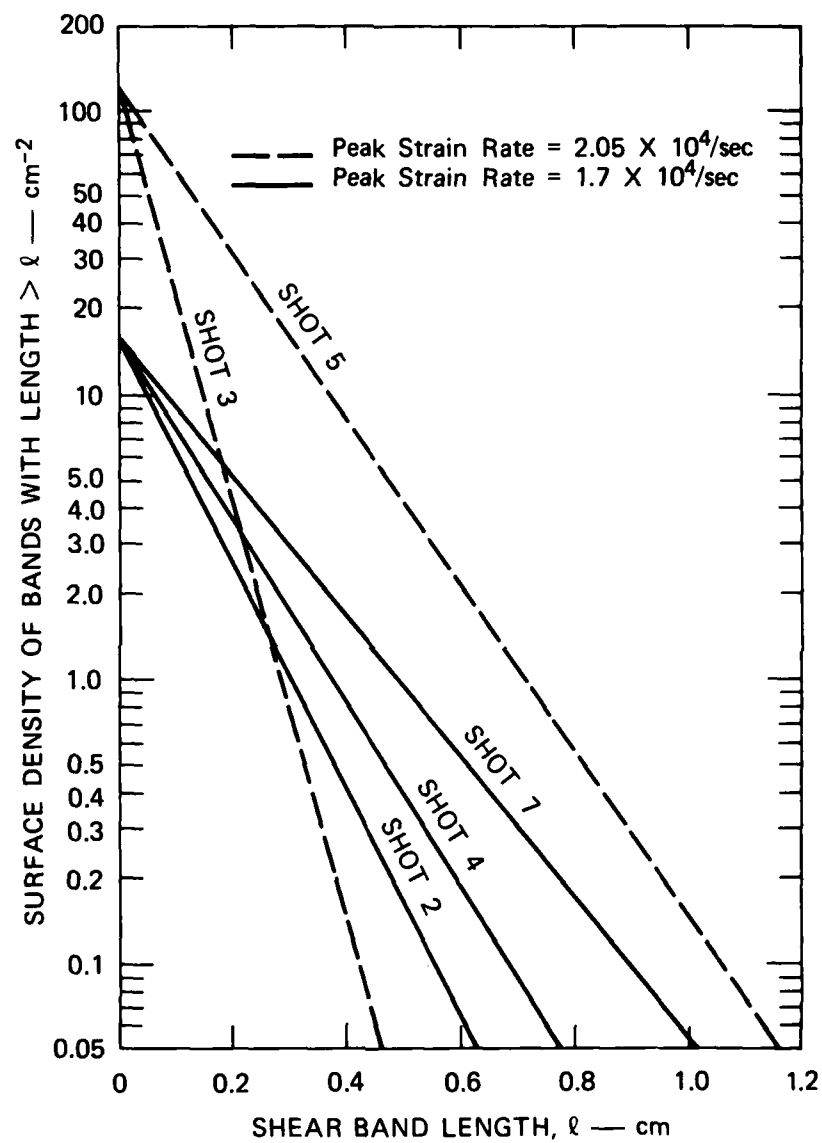
We noticed that the shear band density distribution curves are approximately straight lines in the semi-log graph. So in our first attempt to quantify these qualitative results, and to obtain parameters that would be used in the initial computer simulation in which shear banding was allowed, we fitted the data with straight lines such that lines for experiments with the same peak strain rates have the same y-axis intercept. The results are shown graphically in Figure 19. A consequence of this procedure is that the shear bands follow a viscous growth law of the form

$$\dot{R}/R = \text{constant},$$



MA-6408-18

FIGURE 18 COMPUTED MID-AXIAL MODE 1 PEAK PLASTIC SHEAR STRAIN RATE AS A FUNCTION OF DETONATION PRESSURE



MA-6408-24

FIGURE 19 SHEAR BAND DENSITY DISTRIBUTIONS FORCED TO OBEY VISCOUS GROWTH LAW

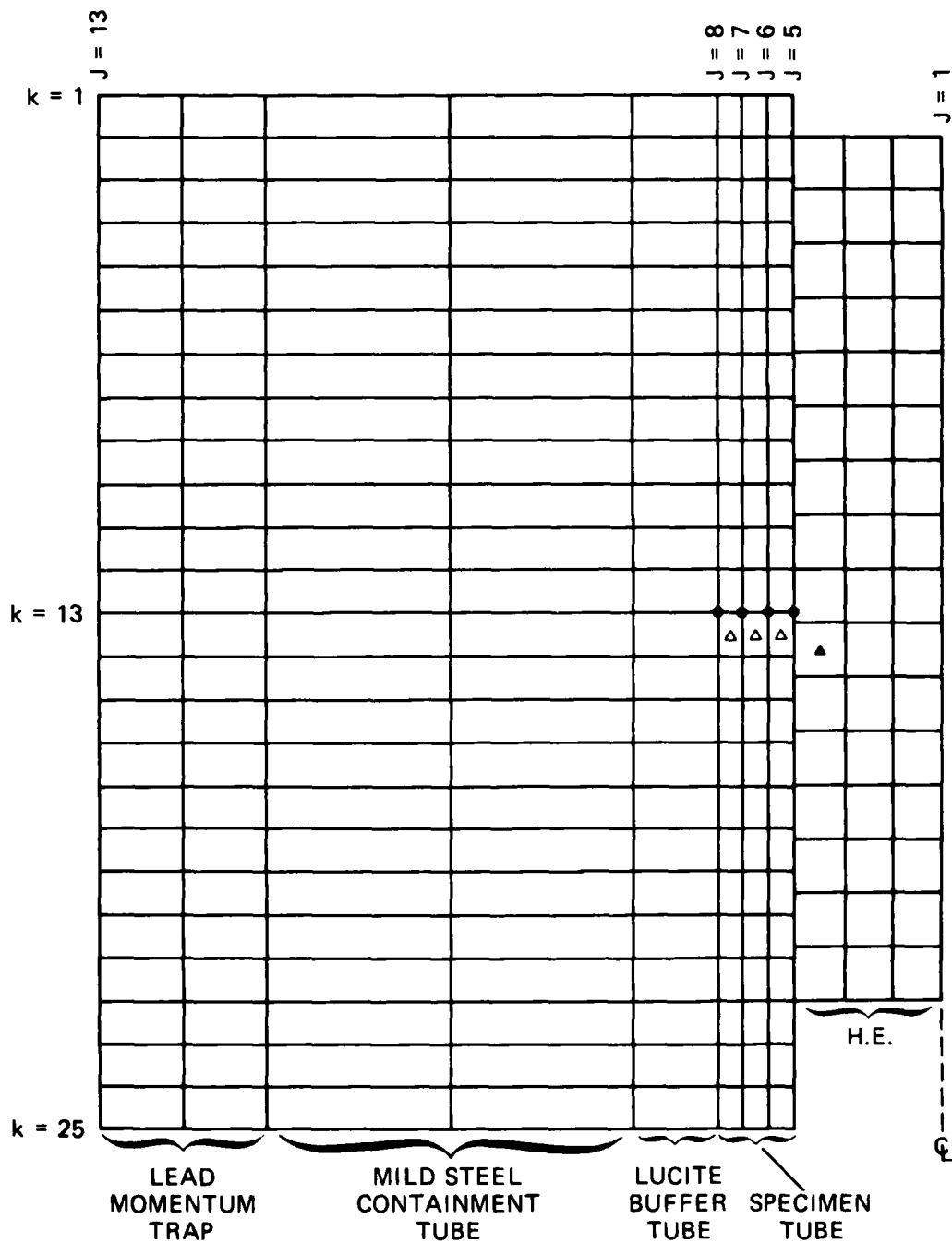
where R is the shear band radius (equal to $\frac{1}{2}l$). This appears at first glance to be in agreement with the growth law assumed in References 1 and 2 and given by Eq. (2) in Section 2. However, the initial evidence suggests that R/R is not a linear function of strain rate, since for the cases shown in Figure 19, $C_g \approx 21$ for $\dot{\epsilon}_{\phi\theta}^{PS} = 2.05 \times 10^4/\text{sec}$, whereas $C_g \approx 8$ for $\dot{\epsilon}_{\phi\theta}^{PS} = 1.7 \times 10^4/\text{sec}$. Subsequent iterative calculations may show that a constant value of C_g can describe the data, but at present it appears R/R will be a more complicated function of strain rate than that given by Eq. (2).

The magnitude of the shear band growth velocity approaches 1.7 mm/ μs for the highest strain rates. This speed is about half the shear wave velocity for 4340 steel (≈ 3.2 mm/ μs), which is the theoretical limit for such instabilities.

As expected, the nucleation rate appears to be a strong function of strain rate. The total surface density of nucleated shear bands (see Figure 19) increases from 16 cm^{-2} to 125 cm^{-2} as the nominal peak strain rate increases from $1.7 \times 10^4/\text{sec}$ to $2.05 \times 10^4/\text{sec}$.

At the very end of the program, after a slide line capability had been inserted into the TROTT code, we re-ran the no-damage calculation of Shot 2, using a slide line to simulate the motion of the explosive gases along the interface with the specimen tube. To illustrate this calculation, we plotted various motions, stresses and strains experienced by the specimen tube at its mid-axial location. The cell layout is shown in Figure 20, along with the location of the cells for which we have plotted the histories. The HE begins detonation simultaneously across the top and the detonation travels downward. Figure 21 shows the pressure* history in the HE cell adjacent to the specimen tube near the mid-axial location. The radial position and velocity histories of the 4 mid-axial cells ($J = 5$ through 8) are shown in Figure 22. The principal stress* histories within the specimen tube (cells $J = 6$ through 8) are

* Note that positive values for pressures and stresses connote compression; negative values connote tension.

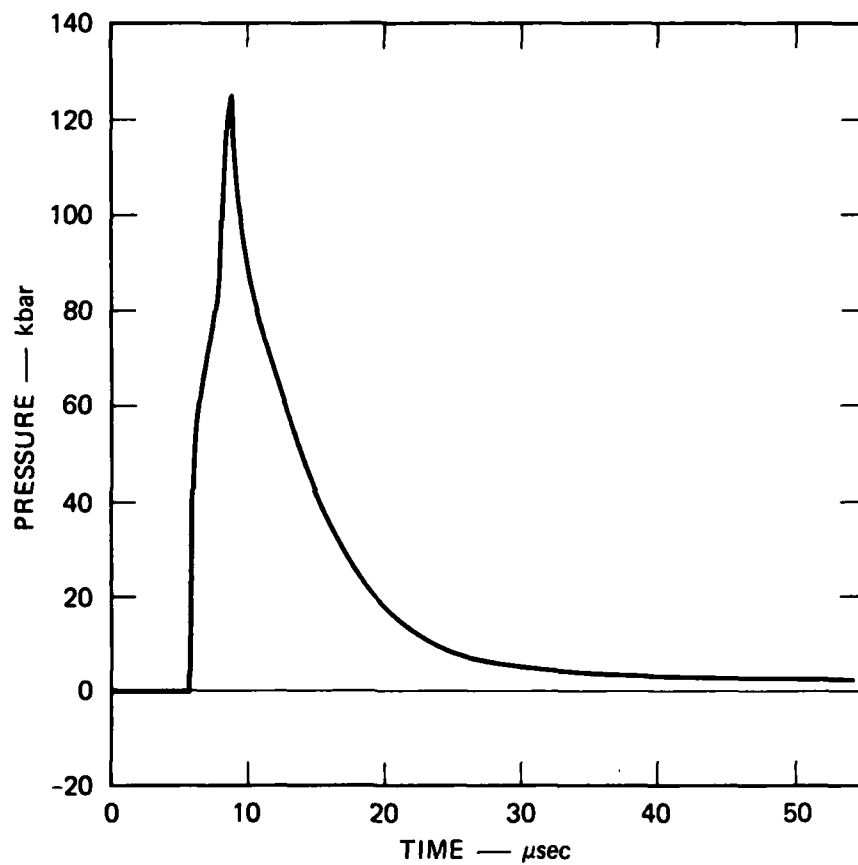


Location of Histories Plotted in Subsequent Figures for:

- Positions and Velocities, Δ Stresses and Strains, ▲ Pressures

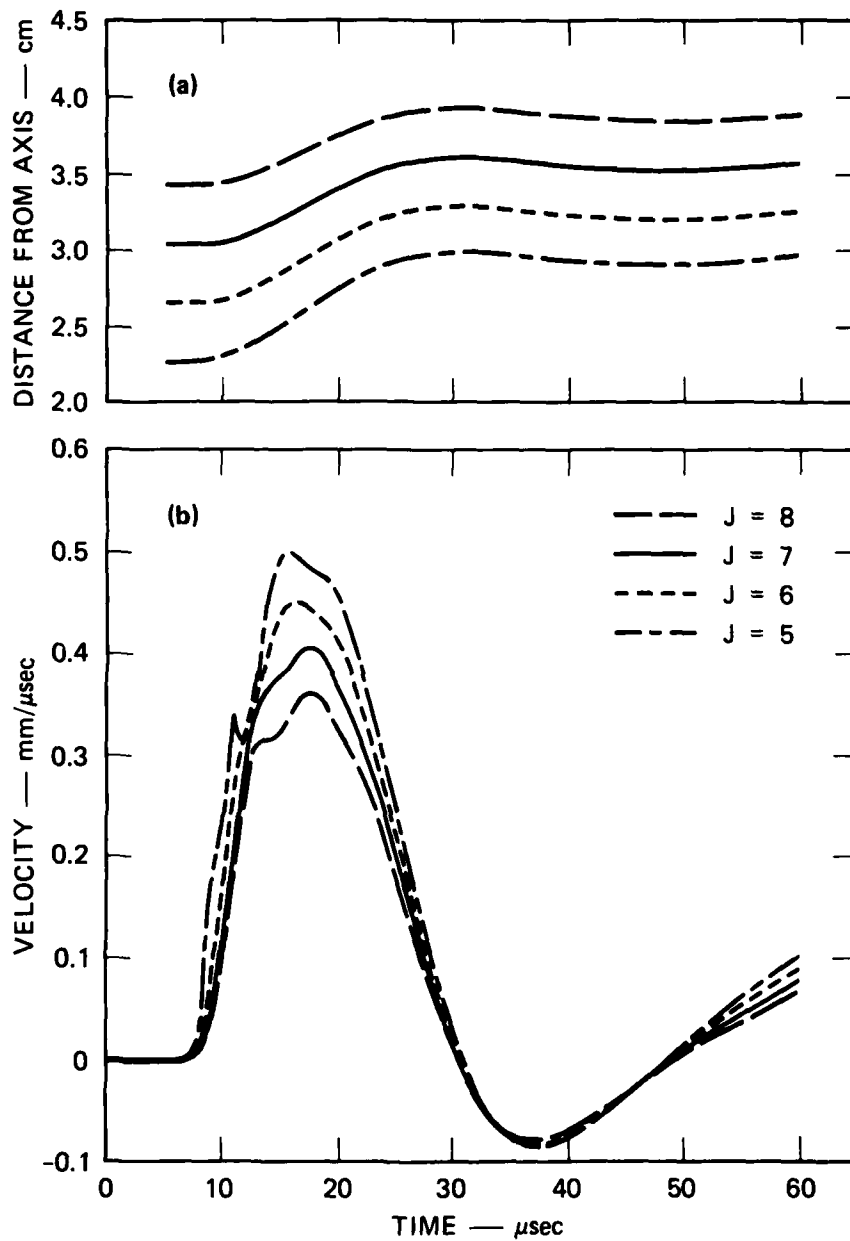
MA-6408-30

FIGURE 20 CELL LAYOUT FOR COMPUTER SIMULATION OF CONTAINED FRAGMENTING CYLINDER EXPERIMENTS



MA-6408-31

FIGURE 21 CALCULATED PRESSURE HISTORY IN THE H.E. ADJACENT TO THE SPECIMEN TUBE NEAR THE MID-AXIAL LOCATION



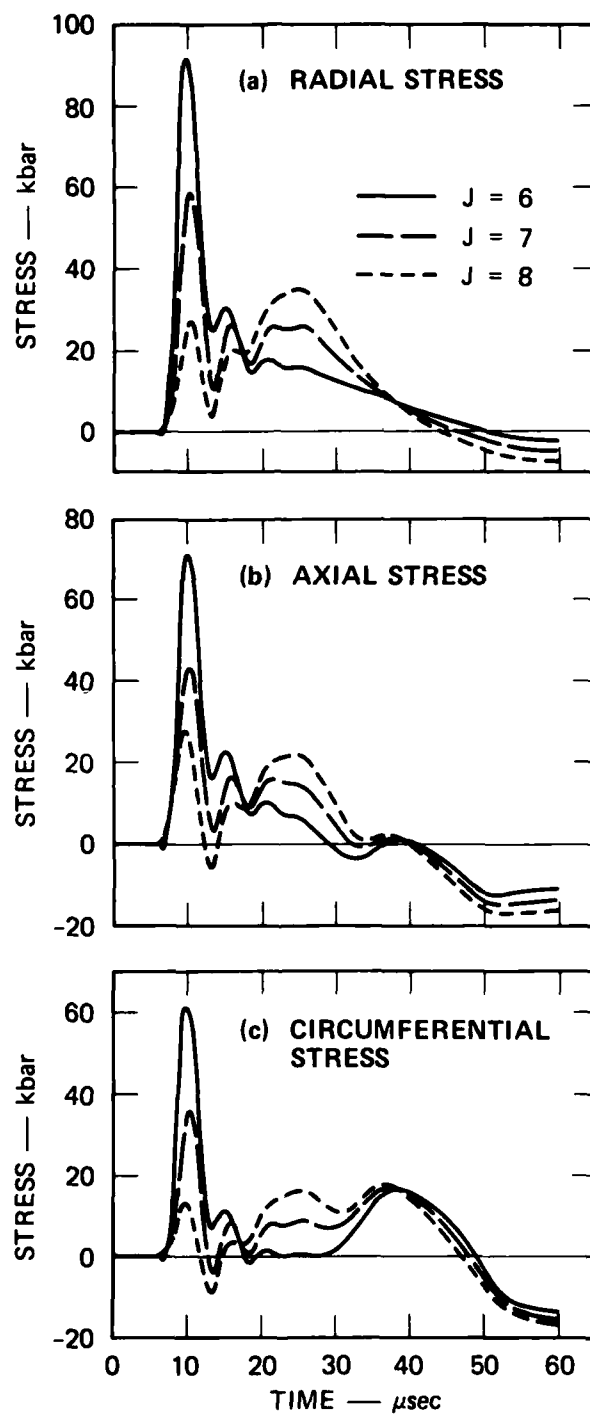
MA-6408-32

FIGURE 22 CALCULATED RADIAL POSITION (a) AND VELOCITY (b) HISTORIES FOR SPECIMEN TUBE AT THE MID-AXIAL LOCATION

are shown in Figure 23. The equivalent plastic strain* histories and the plastic shear strain histories in the mode 1, 2, and 3 directions (as defined in Figure 4) are shown in Figures 24 and 25, respectively.

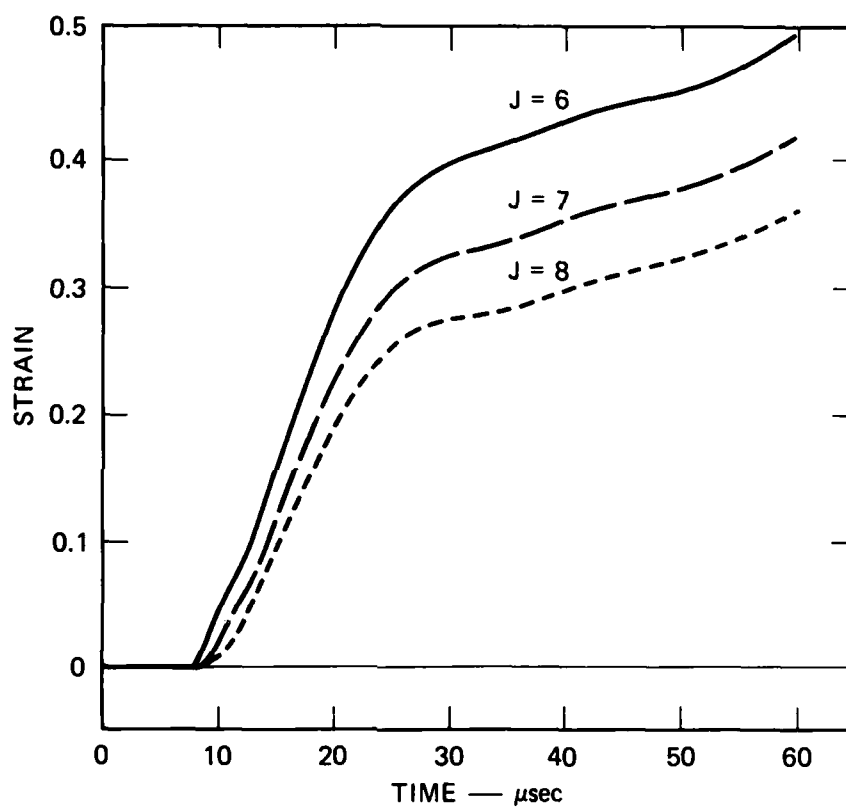
A comparison of this slide-lined calculation with the one described earlier for Shot 2, which lacked a slide line, showed that the slide-lined calculation exhibited a decrease of 10% in a peak Mode 1 shear strain rate, a decrease of 18% in the final Mode 1 shear strain, and an increase of 4% in the final specimen tube thickness. Furthermore, the final tube thickness attained at the mid-axial location in the slide-lined calculation was within 1% of that measured experimentally. Thus, the original calculations without the slide line appear to be approximately valid, as hoped. However, the calculation with a slide line represents a meaningful modification to the contained fragmenting cylinder simulation and should be used as a starting point for future iterative calculations with damage that will be necessary to better define the shear banding nucleation and growth parameters for 4340 steel.

* The equivalent plastic strain is defined as $\sqrt{3/2}$ times the square root of the sums of the squares of the plastic strains in the three principal directions.



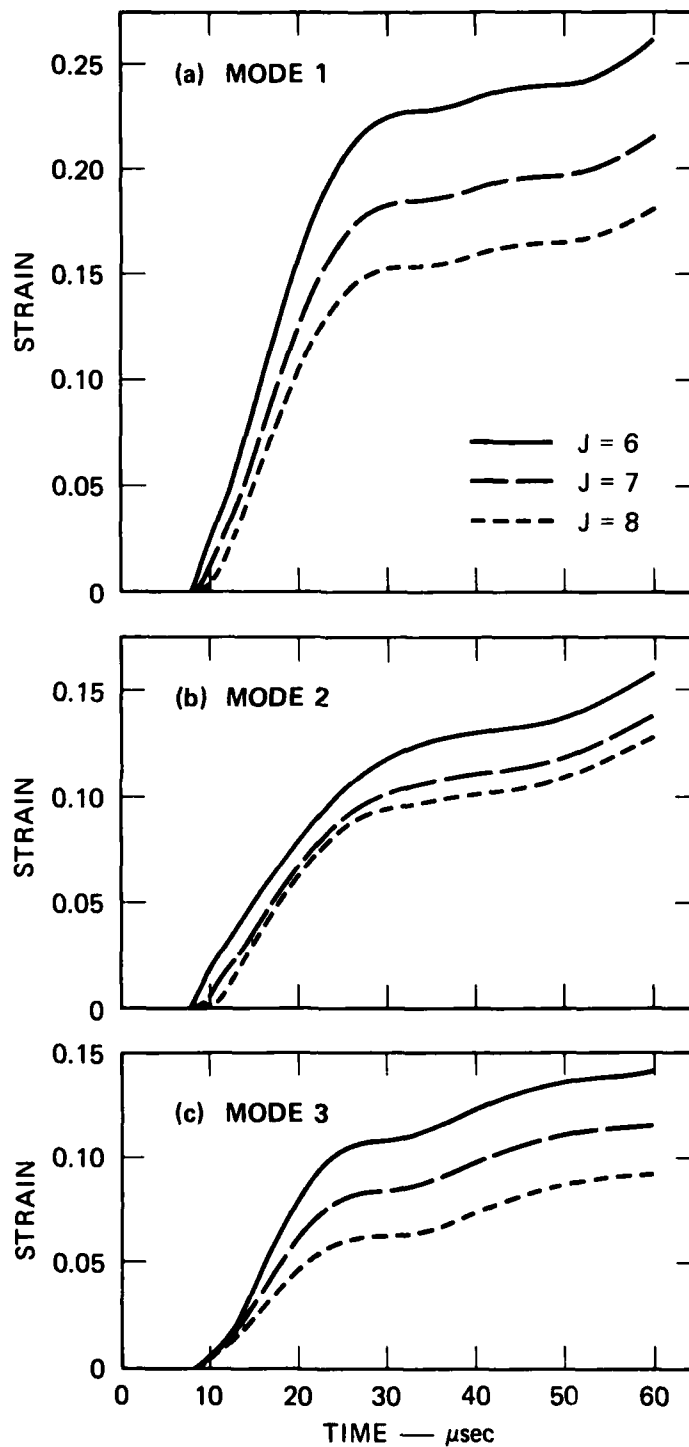
MA-6408-33

FIGURE 23 CALCULATED PRINCIPAL STRESS HISTORIES IN THE SPECIMEN TUBE AT THE MID-AXIAL LOCATION



MA-6408-34

FIGURE 24 CALCULATED EQUIVALENT PLASTIC STRAIN HISTORIES
IN THE SPECIMEN TUBE AT THE MID-AXIAL LOCATION



MA-6408-35

FIGURE 25 CALCULATED PLASTIC SHEAR STRAIN HISTORIES IN THE SPECIMEN TUBE AT THE MID-AXIAL LOCATION

5 SHEAR BAND NUCLEATION THRESHOLD CRITERION

Introduction

In our original development of the SNAG model^{1,2} we did not attempt to determine what causes adiabatic shear bands to form initially. Instead, we constructed a model for the nucleation, growth, and coalescence of the bands once they appeared. The threshold criterion governing the initial appearance, or nucleation, of the bands was estimated empirically, and it stated that shear bands nucleate when both a critical strain and a critical strain rate are exceeded. No derivation was presented. However, such a derivation of a nucleation criterion that depends on other, commonly measured material properties would be very desirable because the propensity of various materials to form shear bands could then be assessed without additional extensive testing.

This section describes our recent efforts to derive and test such a criterion. We first give some background information, then state our postulated criterion, and next derive the mathematical expressions for the nucleation criterion. Finally, we apply the criterion to several steels, and test it against experimental data.

Background

Classical instability analysis is based on assuming the existence of perturbations, and then deriving the conditions for their growth.^{7,8} The usual result for plasticity problems is that shear instabilities will occur when increasing strain results in decreasing load, that is, where the work hardening coefficient becomes zero or negative. However, instabilities with positive work hardening coefficients have been shown to be possible by Rudnicki and Rice⁹ and by Asaro and Rice.¹⁰ A recent review of these results has been given by Rice.¹¹

The above instabilities are basically static, whereas experimental evidence suggests that adiabatic shear band initiation requires high strain rates. However, plastic instabilities can also be viewed dynamically.^{8,11} For strains equal to or larger than the critical value, the plastic shear wave velocity becomes zero or imaginary. Such strains cannot be propagated away from the region of load application, and the deformation becomes localized as a growing perturbation. The classical example of such an instability is that first investigated independently during the Second World War by von Karman, Taylor, White, Le Van Griffis, Rakhmatvolin, and Shapiro. A review of their work is given by Davies.¹² The above workers found that for wires subjected to tensile impact, strains larger than that corresponding to the ultimate strength cannot be propagated, and the strain is localized at the impact end of the wire, where necking occurs.

It is clear that this dynamic instability is closely related to the static necking instability. The usual language used to describe the necking instability is that for strains larger than those at ultimate tensile strength (UTS), the decrease in load due to the reduction in area exceeds the increase in load due to work hardening, thus causing decreasing load with increasing displacement, and fulfilling the condition for a plastic instability. However, because the Lagrangian plastic bar velocity, $\left(\frac{1}{\rho_0} \frac{\partial \sigma}{\partial \epsilon}\right)^{\frac{1}{2}}$ (where σ and ϵ are engineering stress and strain), is the governing wave velocity in this problem, the strain at UTS is also the strain for which the wave velocity becomes imaginary.

For static or dynamic compression of a rod, however, there is no corresponding "barreling" instability because the force-displacement curve always has a positive slope. Nonetheless, extremely localized "barreling" of impact rods is often observed. This occurs because the bar velocity can become small compared to the impact velocity, even though it is non-zero. Thus, the larger strains do not propagate very far down the rod during the duration of the load. This phenomenon is therefore a strain localization without being an instability. Nevertheless, the dynamic localization process is the same in both cases: "trapping" of the plastic wave.

Postulated Nucleation Criterion

We postulate that adiabatic shear banding is a dynamic phenomenon whereby plastic strain localization at a perturbation first occurs by "trapping the plastic wave," and is then followed by thermal softening as the imposed global deformation is accommodated solely within the perturbation, thus concentrating the plastic work and the associated heating. Hence, our postulated initiation mechanism is not restricted to cases of zero or negative work hardening (or to the static cases with positive work hardening discussed by Rice and coworkers) but is a purely dynamic phenomenon. It can, however, be considered as an extension of the usual perturbation approach to account for the finite rate at which plastic flow can occur.

We thus formulate the shear band initiation criterion as follows: Plastic shear localization leading to shear banding may occur at perturbations when the rate of applied shear deformation exceeds the ability of the plastic shear wave to transmit significant deformation to adjacent material. This criterion will allow dynamic localization to occur when there is positive work hardening because the rate of applied deformation is non-zero. For quasistatic loads, the rate of applied deformation is nearly zero, and the above criterion will reduce to the usual static one of zero or negative work hardening.

The above criterion is only a necessary condition; an associated requirement is that the shear stress-strain curve must have a zero or negative second derivative. That is, the plastic wave velocity must remain constant or decrease with increasing strain. Otherwise, there could be a "shocking-up" effect that might prevent wave trapping. Further, the wave trapping must be severe enough to cause significant thermal softening. Nevertheless, we shall assume for the present that the necessary condition is the primary initiation criterion.

Relation of Material Properties to Flow Field Velocities

The above criterion can be quantified by considering the type of deformation shown in Figure 26. We assume that a perturbation in an otherwise smoothly varying strain field exists in the x_1, x_3 plane and is represented by the area A in that plane. Across this perturbation at a time $t = 0$, there is a discontinuous jump in shear strain. For simplification, we assume that in the vicinity of the perturbation, all of the displacement is in the x_1 , direction, and is given by

$$u_1 = x_1 - h_1, \quad (3)$$

where

$$x_1 = \hat{x}_1(h_1, t) \quad (4)$$

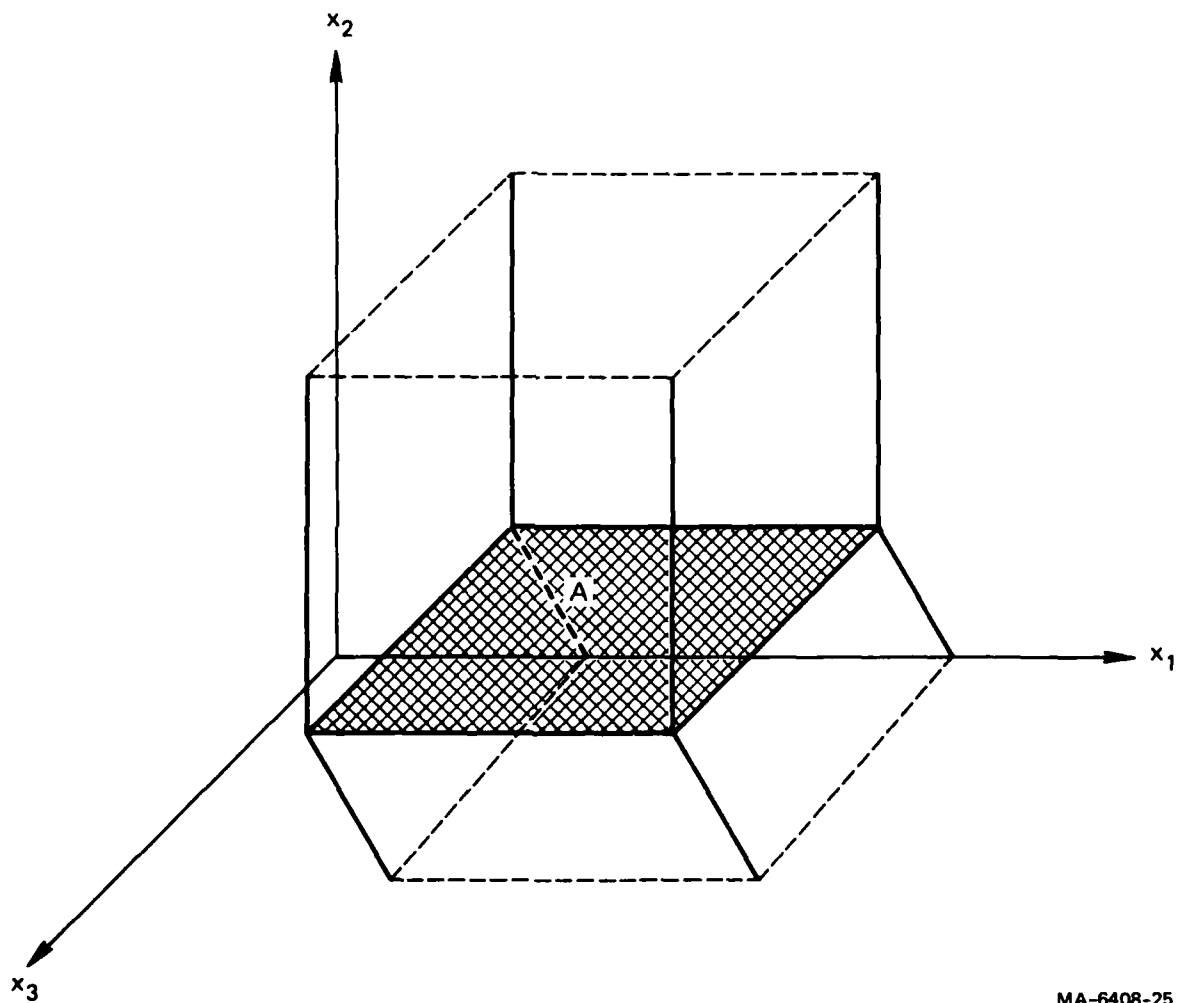
and $h_1 \equiv$ Lagrangian position coordinate .

The Lagrangian shear strain, particle velocity, and shear strain rate are defined by

$$\begin{aligned} \gamma_{12} &= - \partial u_1 / \partial h_2 \\ v_1 &= \partial u_1 / \partial t \\ \dot{\gamma}_{12} &= - \partial v_1 / \partial h_2 \end{aligned} \quad (5)$$

Thus, the differential displacement may be written

$$du_1 = \frac{\partial u_1}{\partial h_2} dh_2 + \frac{\partial u_1}{\partial t} dt = - \gamma_{12} dh_2 + v_1 dt. \quad (6)$$



MA-6408-25

FIGURE 26 DEFORMATION ACROSS A PERTURBATION IN THE SHEAR STRAIN FIELD

The Lagrangian propagation velocity associated with a constant value of u_1 is therefore

$$c_{u_1} \equiv \left(\frac{\partial h_2}{\partial t} \right)_{u_1} = - \frac{\partial u_1 / \partial t}{\partial u_1 / \partial h_2} = \frac{v_1}{\gamma_{12}} \quad (7)$$

Similar arguments show that paths of constant particle velocity v_1 and shear strain γ_{12} have the velocities

$$c_{v_1} = - \frac{\partial v_1 / \partial t}{\partial v_1 / \partial h_2} = \frac{\dot{v}_1}{\dot{\gamma}_{12}} \quad (8)$$

and

$$c_{\gamma_{12}} = - \frac{\partial \gamma_{12} / \partial t}{\partial \gamma_{12} / \partial h_2} = - \frac{\dot{\gamma}_{12}}{\partial \gamma_{12} / \partial h_2} \quad (9)$$

respectively.

These velocities simply describe the dynamic deformation field, and do not contain information about material properties. The material properties enter through a constitutive relation:

$$\tau_{12} = \hat{\tau}_{12}(\gamma_{1j}) \quad (10)$$

where τ_{12} is the shear stress in the h_1 direction across the perturbation plane represented by A in Figure 26. Then we write the conservation of momentum equation in Lagrangian coordinates:

$$\rho_o (\partial v_1 / \partial t)_{h_2} + (\partial \hat{\tau}_{12} / \partial h_2)_t = 0.$$

In the vicinity of the perturbation A, this can be written with the aid of (N8) as

$$\rho_o (\partial v_1 / \partial t)_{h_2} + (\partial \hat{\tau}_{12} / \partial \gamma_{12})_t (\partial \gamma_{12} / \partial h_2)_t = 0, \quad (11)$$

because near the perturbation all strains except γ_{12} are zero.

Substituting the expressions for v_1 and γ_{12} from (5) into (11), yields

$$\frac{\partial^2 u_1 / \partial t^2}{\partial^2 u_1 / \partial h_2^2} = C_p^2 = \frac{H}{\rho_o} \quad (12)$$

$$\text{where } C_p^2 \equiv \frac{1}{\rho_o} \left(\frac{\partial \hat{\tau}_{12}}{\partial \gamma_{12}} \right)_t \equiv H / \rho_o, \quad ,$$

and H is the local hardening modulus. An identity arising from the definitions (5), (8), and (9) is:

$$C_{v_1} C_{\gamma_{12}} = \frac{\partial^2 u_1 / \partial t^2}{\partial^2 u_1 / \partial h_2^2} \quad (13)$$

Comparison of (12) and (13) yields the important link between the deformation field and the work hardening curve of the specific material:

$$C_{v_1} C_{\gamma_{12}} = C_p^2 = H / \rho_o \quad (14)$$

Examination of Flow Field for Wave Trapping

To define the conditions for wave trapping, we assume that the perturbation surface represented by A in Figure 26 is located at $h_2 = h_o$. At $t = 0$ unstrained material on one side of the perturbation

is separated from material at a finite strain γ_{12} on the other side of the perturbation. We further assume that the constitutive relations are the same for the material on each side of the perturbation.

This strain discontinuity introduced at $t = 0$ will cause waves to propagate away from the perturbation surface. These waves can be plotted in terms of the flow variables: displacement, strain, and particle velocity. If wave trapping is to occur, the strain must tend to remain localized at the perturbation surface, and only diffuse slowly away. That is, the perturbation acts as a kind of piston; we are interested in the case when the imposed strain remains trapped at the piston.

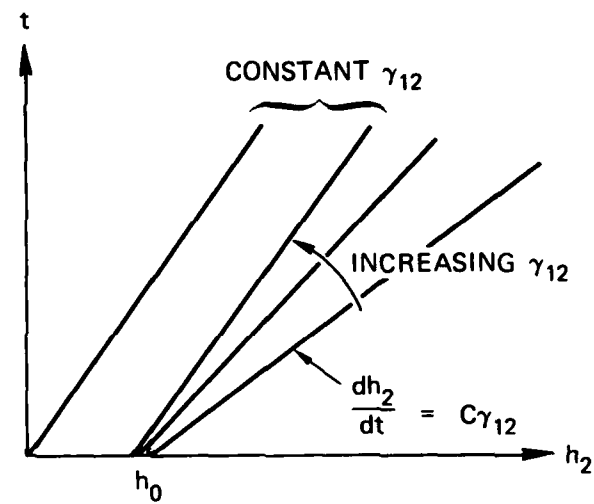
This situation is diagrammed in Figure 27. In 27(a) lines of constant strain are plotted in h_2, t space, and in 27(b) the corresponding profiles in h_2, γ_{12} space are shown at successive times. In the situation shown, the peak strain behind the perturbation surface propagates more slowly into the initially unstrained material than do the lower strains, in a diffusion-like process.

This situation can also be represented in terms of the displacement field, u_1 , as shown in Figure 28, which plots lines of constant u_1 radiating away from the perturbation surface. The dh_2/dt slopes of the lines are the values of C_{u_1} . The gradient of the lines in the h_2 direction is $-\gamma_{12}$, and the gradient in the t direction is v_1 . We see that

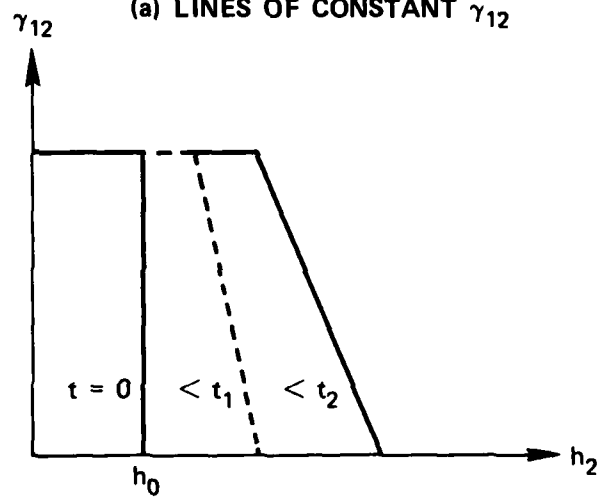
$$\begin{aligned} (\partial C_{u_1} / \partial h_2)_{t_1} &\geq 0 \\ (\partial C_{u_1} / \partial t)_{h_2} &\leq 0 \end{aligned} \tag{15}$$

We note that in the region of constant strain, the lines of constant u_1 are parallel and travel more slowly than the lines of lower displacement. This corresponds to the diffusion-like propagation of strain shown in Figure 27(a), from which we see that

$$\begin{aligned} \partial \gamma_{12} / \partial h_2 &\leq 0 \\ \partial \gamma_{12} / \partial t &\geq 0 \end{aligned} \tag{16}$$



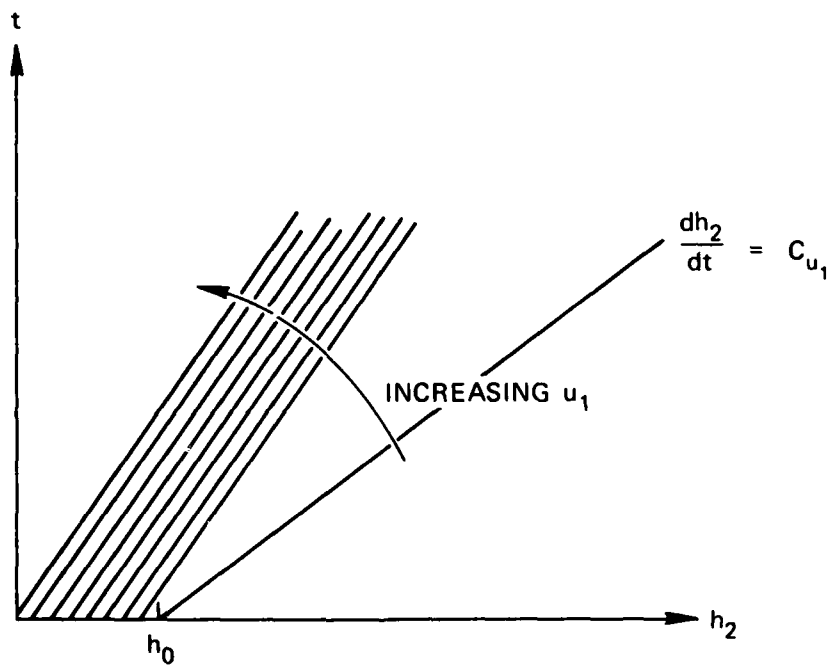
(a) LINES OF CONSTANT γ_{12}



(b) PROFILES AT SUCCESSIVE TIMES

MA-6408-21

FIGURE 27 EXAMPLE OF CASE WHERE PLASTIC WAVE TRAPPING OCCURS



NOTE: Each path line represents a constant increment in u_1 from that on the adjacent line.

MA-6408-22

FIGURE 28 PATH LINES OF CONSTANT DISPLACEMENT u_1
FOR CONDITION OF LOCALIZATION

We next combine the inequalities (15) and (16) with the definitions (5) to obtain a criterion for wave trapping.

First, from the first of the inequalities (15), and from (7), we obtain

$$\gamma \partial v / \partial h \geq v \partial \gamma / \partial h , \quad (17)$$

where the subscripts have been dropped for convenience. Similarly, from the second of the inequalities (15) we obtain

$$\gamma \partial v / \partial t \leq v \partial \gamma / \partial t \quad (18)$$

Since γ is positive, (17) and (18) can be written as

$$- \partial \gamma / \partial t \geq C_u \partial \gamma / \partial h \quad (19)$$

and

$$\partial v / \partial t \leq C_u (-\partial v / \partial h) , \quad (20)$$

respectively, where we have used (7) to define C_u . Finally, since (16) shows that $\partial \gamma / \partial h$ is negative and $\partial \gamma / \partial t$ is positive, (19) and (20) can be written as

$$C_\gamma \leq C_u , \quad (21)$$

and

$$C_v \leq C_u , \quad (22)$$

respectively, where we have used (8) and (9).

If we now multiply (22) by C_γ , we obtain

$$C_\gamma C_u \geq C_p^2 , \quad (23)$$

where we have used (13) and the fact that C_γ is positive. Relation (23) is the one we shall use as the necessary condition for adiabatic shear band nucleation.

Another type of dynamic localization occurs not at the "piston," but in a shock front. If the strain increment introduced at the perturbation had propagated away as a shock, or discontinuous jump in strain, followed by a decaying tail, it can be shown that the inequalities (15) are unchanged, but the sense of inequalities (16) are reversed. This would cause a reversal of the inequality (23).

Thus, if an equal sign replaces the inequality sign in (23), the resultant equation defines a critical load curve, as illustrated in Figure 29. Above the curve, wave trapping at the perturbation can occur. Below the curve, perturbations are carried away from the perturbation to localize in a shock front. That is, above the curve deformations tend to accumulate at the piston (perturbation), and below the curve they tend to accumulate in a shock front. On the curve, the waves are neither dispersive or convergent, and the perturbation is propagated unchanged as in an elastic material.

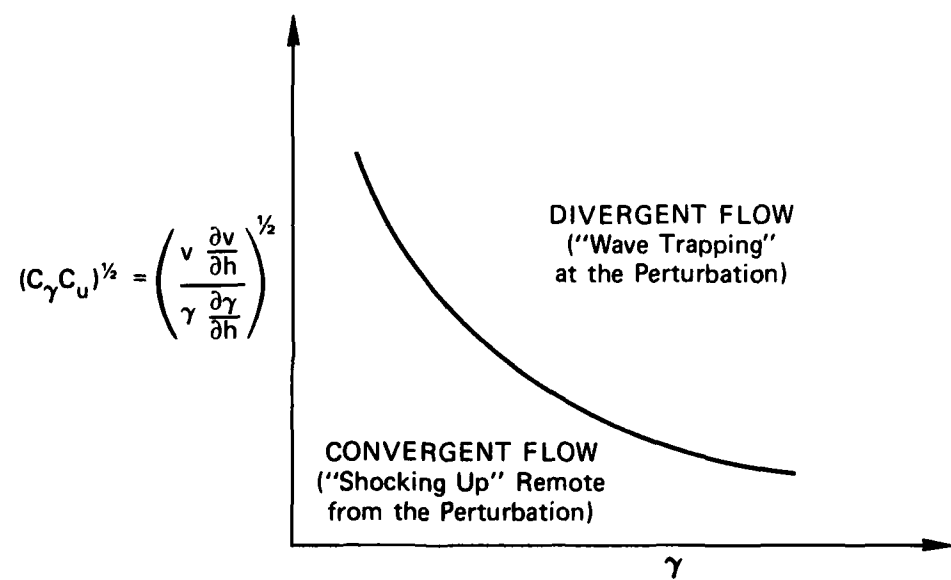
Application of the Criterion to Steel

To apply the above concept to steels, we use the common expression for the work hardening curve,

$$\tau = \tau_o \gamma^n \quad (24)$$

where τ and γ are now regarded as scalar quantities expressed in terms of suitable invariants of the stress and strain tensors and τ_o and n are material parameters fitted to experimental data. We thus assume isotropic materials. The value of C_p , or $(H/\rho_o)^{\frac{1}{2}}$, is then taken to be

$$C_p = \left(\frac{1}{\rho_o} \frac{\partial \tau}{\partial \gamma} \right)^{\frac{1}{2}} = \left(\frac{n \tau_o}{\rho_o} \right)^{\frac{1}{2}} \gamma^{\frac{n-1}{2}} \quad (25)$$



MA-6408-23

FIGURE 29 CRITICAL LOAD CURVE FOR DYNAMIC LOCALIZATION

We next write (23) as:

$$(C_{\gamma} C_u)^{\frac{1}{2}} = \left| \frac{v \partial v / \partial h}{\gamma \partial \gamma / \partial h} \right|^{\frac{1}{2}} \geq \left(\frac{n \tau_o}{\rho_o} \right)^{\frac{1}{2}} \left| \frac{n-1}{\gamma} \right|^{\frac{1}{2}} \quad (26)$$

where we have used absolute values to avoid confusion about the direction of the inequalities. Table 2 lists representative values of τ_o , n , and ρ for three steels,* and Figure 30 shows the corresponding critical load curves.

Table 2
MATERIAL PROPERTIES FOR SEVERAL STEELS

Material	$\tau_o \left(\frac{\text{dyne}}{\text{cm}^2} \right)$	n	$\rho_o \text{ (g/cc)}$	$\left(\frac{n \tau_o}{\rho_o} \right)^{\frac{1}{2}} \text{ (cm/s)}$
Armco Iron	5.3×10^9	0.26	7.8	1.3×10^4
HF-1 steel	1.57×10^{10}	0.10	7.8	1.4×10^4
4340 steel	3.3×10^{10}	0.15	7.8	2.5×10^4
RHA (1.5" plate)	1.2×10^9	0.08	7.8	3.5×10^3

*The data for 4340, R_C53 steel were generated at SRI; the RHA steel data for the 1.5" plate were taken from R. F. Benck, BRL Memorandum Report No. 2703, November 1976; and the HF-1 and Armco iron data were estimated from data given for similar steels in G. E. Dieter, Mechanical Metallurgy, McGraw-Hill, N.Y. (1961), p. 248.

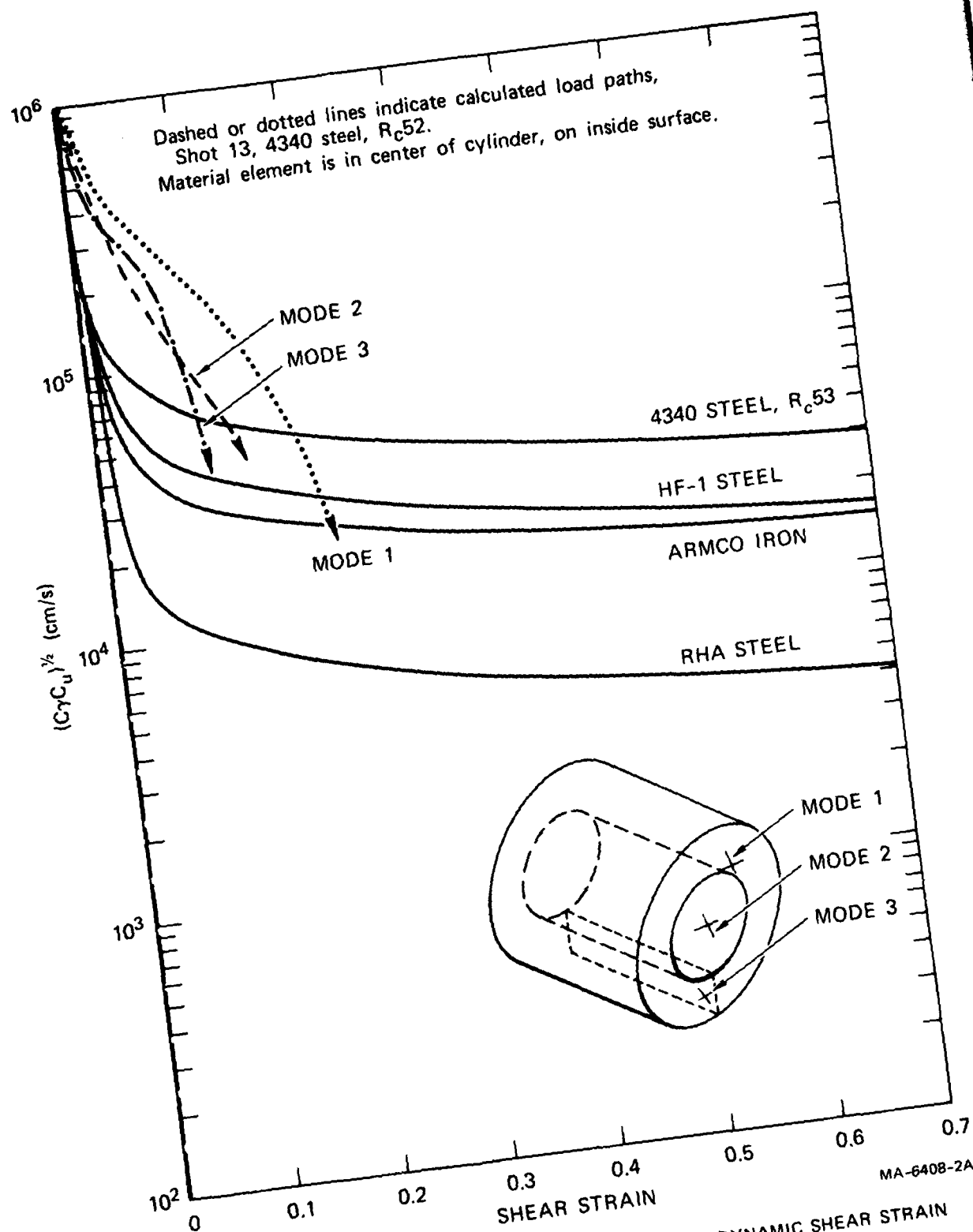


FIGURE 30 CRITICAL LOAD CURVES FOR LOCALIZATION OF DYNAMIC SHEAR STRAIN

These critical load curves were calculated from quasistatically measured values of τ_0 and n in Eq. (24). The dynamic work hardening curves, corresponding to the strain rates of 10^4 s^{-1} often encountered in shear banding experiments, may be significantly different for some materials. Unfortunately, data for these steels in the high strain rate region are sparse, although impact data by Jones et. al.¹³ suggest that the yield strength of 4340 steel is not very rate-dependent. Hence, the critical load curves plotted in Figure 30 may be in error.

Comparison With Experimental Data

We checked the plausibility of the above initiation criterion by comparing the critical load curve for 4340, $R_C 53$ steel with calculated $(C_Y C_U)^{\frac{1}{2}}$ versus γ paths taken by material elements in exploding cylinder experiments that bracketed the threshold conditions for shear banding. Shots 13, 15, and 16 on 4340, $R_C 52$ steel all spanned the range from no shear banding in some orientation modes to shear banding in other orientation modes.

In Shot 13, material on the inside surface of the cylinder exhibited incipient shear band striations in the mode 1 orientation, but none in the mode 2 and 3 orientations. For this material element we computed $(C_Y C_U)^{\frac{1}{2}}$ and γ histories for each orientation, and plotted the $(C_Y C_U)^{\frac{1}{2}}$ versus γ paths in Figure 30.

In contrast to Shot 13, which showed only incipient mode 1 banding, Shot 15 showed significant banding in the mode 1 orientation. A few mode 2 bands were found; these showed very little growth. No mode 3 loads were seen. The corresponding load paths are shown in Figure 31. Comparison with Figure 30 shows that in Shot 15 the load paths for all modes were shifted toward higher strains, but are otherwise very similar to the paths for Shot 13.

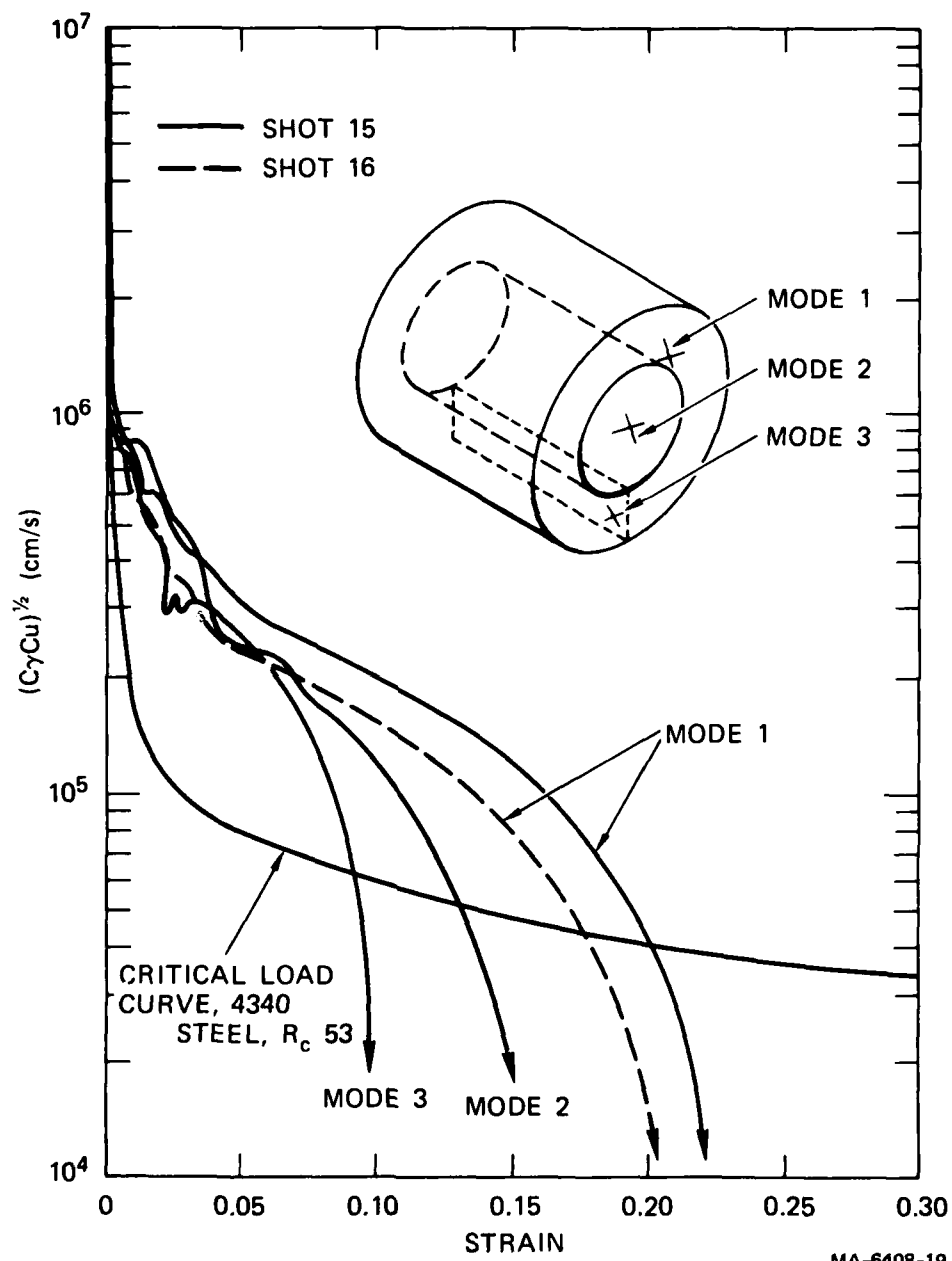


FIGURE 31 DYNAMIC LOAD PATHS FOR SHOTS 15 AND 16

Finally, Shot 16, performed at somewhat lower strain rates, showed two long axial cracks completely through the cylinder. One of these cracks was definitely a mode 1 shear band. We conclude that mode 1 shear banding occurred in this experiment; the mode 1 load path is shown as the dashed curve in Figure 31.

These results are summarized in Figure 32, which compares all the load paths for shear banded and non-shear banded material from Shots 13, 15, and 16.

Figure 32 shows that the load paths for material that nucleated shear bands are consistently above those for which nucleation was not observed, as expected. However, all the load paths have portions above the critical load curve, suggesting that nucleation should have occurred in every case.

There are two effects that could help resolve this discrepancy. First, as discussed above, the dynamic critical load curve may lie above the static curve shown in Figure 32. Second, shear band growth as well as nucleation is required before the bands can be observed. Our preliminary evaluation of growth velocities suggests that the growth law is approximately given by Eq. (2) in Section 2, with C_g being on the order of 10.

Thus,

$$R/R_o \cong \exp (10\epsilon_{\phi\theta}^{PS}) , \quad (27)$$

and the relative growth increases from about 3 for strains of 0.1 to more than 7 for strains of 0.2. At still higher strains the growth increases dramatically. Thus, the observed transition from no shear banding to significant shear banding also corresponds roughly to the strain levels at which significant growth begins. This is consistent with the observed small sizes of the mode 2 bands in Shot 15.

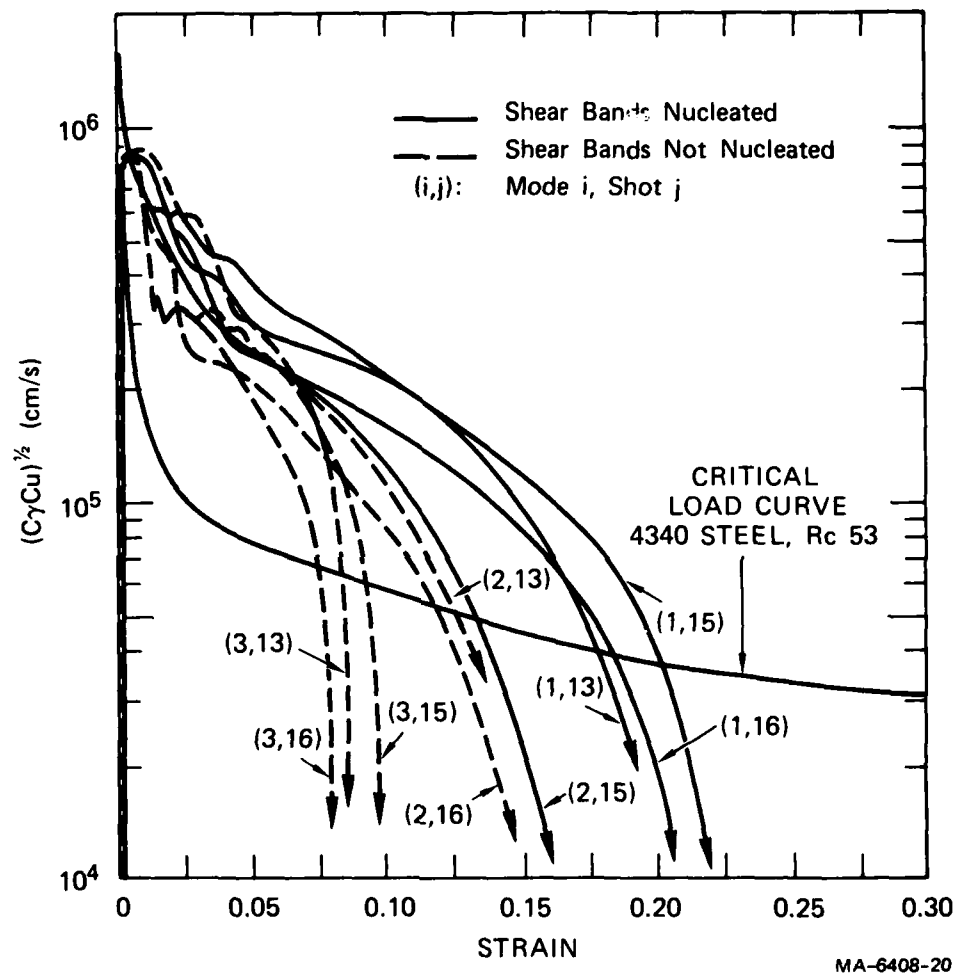


FIGURE 32 COMPARISON OF LOAD PATHS FOR SHEAR BANDED AND NON-SHEAR BANDED MATERIAL

Discussion of Postulated Initiation Criterion

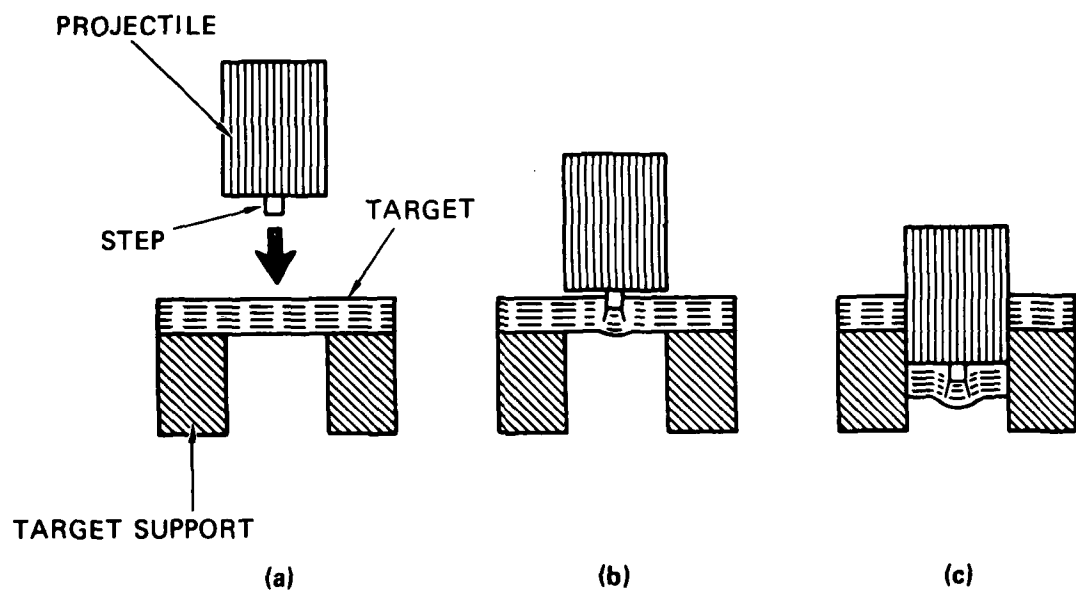
The postulated initiation criterion based on plastic wave trapping appears at this stage to be plausible, but requires further investigation. In future work we will attempt to obtain dynamic stress-strain data for construction of dynamic critical load curves. We will also attempt to further improve the growth law by analyzing additional shear band size data.

6 SIMPLIFIED TESTS TO OBTAIN SHEAR BANDING DATA

We examined a number of experimental techniques that have been used or proposed for use in studying shear banding phenomena. We evaluated the techniques for their ability to provide data, at minimal time and expense, from which we could obtain the parameters required as input to our shear band model. These parameters are basically a threshold or initiation parameter (to specify if the loading conditions allow shear bands to form), a nucleation parameter (to specify the number or density of bands that have been formed), and a growth parameter (to specify the growth velocity of the bands). These three parameters are functions of loading conditions (e.g., the plastic shear strain rate), and the amount of damage is related to the duration of this applied load. To obtain the shear band parameters, one needs an experimental technique in which magnitude and duration of the loading can be varied more or less independently.

In addition to the contained fragmenting cylinder technique described in detail in Section 3, there are a number of other experimental techniques for producing shear bands in the laboratory. They can be divided into three broad classes of techniques: dynamic punch tests, dynamic torsion tests, and high-speed machining tests.

The dynamic punch tests include all forms of impact or penetration experiments, in particular those using a flat-nosed cylindrical projectile, wherein shear banding in the target parallel to the impact direction is the cause of target failure.¹⁴ The most promising technique of this type appears to be the "stepped" projectile technique, described by Wingrove¹⁵ and shown schematically in Figure³³. The magnitude and duration of the load can be varied independently by altering the impact velocity and step length, respectively. This technique was used successfully to study shear banding in aluminum targets impacted by hardened steel penetrators. However, the shear load is concentrated in such a



MA-6408-26

FIGURE 33 SCHEMATIC OF WINGROVE'S STEPPED PROJECTILE TECHNIQUE ¹⁵

Stepped projectile is fired at supported target (a). Step penetrates target (b) until depth of penetration equals step length. Then projectile body impacts target, "freezes" step penetration, and shears out large plug (c) for soft recovery.

narrow region that it is extremely difficult to measure or calculate the stress or strain states existing in that region. Therefore, although it may be possible to obtain a predictive capability for flat-nosed penetration, one could not obtain the parameters necessary for a general shear band model that would be useful in other geometries. Furthermore, this technique may not be suitable for use with an armor steel as the target material because of large deformation in the penetrator. Nevertheless, this technique is valuable in identifying phenomenology for armor penetration applications.

Dynamic torsion tests with thin-walled tubular specimens¹⁶ have been used to generate shear bands in steel at shear strain rates of $\approx 10^2$ /sec. The loading magnitude and duration can be varied by changing the angular velocity and maximum angular stroke of the torsional testing machine. However, the maximum strain rates of machines of this type are orders of magnitude lower than the rates found in exploding rounds or penetration experiments. This is a serious drawback, because shear bands are very sensitive to strain rate.

High-speed machining of metal has been used to study shear band formation,¹⁷ and may in the future be used to measure the temperatures generated during the shear band process.¹⁸ However, the extreme load concentration in the region of band formation is also the major drawback to use of this technique for generating shear band model parameters.

Our present conclusion is that the contained fragmenting cylinder tests provide the most unambiguous data for shear band modeling. The loads and strains are evenly and smoothly distributed over the specimen, thus allowing use of a maximum volume of material in a single test. Furthermore, the simple geometry lends itself to computer modeling. For these reasons, we recommend that this method be used to obtain shear banding parameters for any material that can be obtained in tubular form. However, these tests should be supplemented by tests that approximate the geometrical constraints of the applications of interest. For example, for armor penetration with long rod penetrators, dynamic punch tests are valuable for identifying the key phenomenological processes.

7 DISCUSSION AND RECOMMENDATIONS

The experimental program has fulfilled our objective of providing a data base for 4340 steel that allows improvement of the SNAG model. Data from expanding cylinder tests now exist for three hardnesses of 4340 steel, spanning shear banding levels of damage from incipient shear banding to complete fragmentation. For one hardness ($R_c 40$), quantitative number, size, and orientation distributions for the shear bands were measured and correlated with calculated strain and stress histories. These correlations suggest that strain rate is indeed the key loading parameter that governs the number and growth of the shear bands. Furthermore, our derived nucleation threshold condition suggests that the shape of the dynamic work hardening curve is crucial for determining the strain and strain rate conditions required to nucleate the bands.

The above results indicate that the following future work is highly desirable:

- Complete the quantitative data analysis by measuring the shear band size and orientation distributions for the $R_c 52$ cylinders.
- Measure the static and dynamic stress-strain curves for all three hardnesses. According to Jones et. al., (Ref. 13) 4340 steel may not be excessively rate-dependent, but this should be checked, at least at rates attainable on standard tensile testing machines.
- Continue to analyze the data with iterative computations to obtain the SNAG parameters as functions of the strain hardening curve.
- Perform dynamic punch tests and computer simulations for targets with each of the three hardness levels to see if the SNAG parameters developed from expanding cylinder tests will correctly predict and rank the phenomenology of shear banding in geometries applicable to armor penetration.

The above tasks are needed to fully use the experimental data base generated in this program; they will provide an understanding of how the shear banding process depends on key material properties for one material. Such an understanding is required to allow extrapolation to other materials such as those used for armor and penetrators.

REFERENCES

1. D. C. Erlich, L. Seaman, D. A. Shockey, and D. R. Curran, "Development and Application of a Computational Shear Band Model," SRI Final Report, Contract No. DAAD05-76-C-0762, U.S. Army Ballistic Research Laboratories, Aberdeen Proving Ground, Maryland (May 1977).
2. L. Seaman, D. A. Shockey, D. R. Curran, and R. E. Tokheim, "Development of a Shear Band Model for Fragmentation in Exploding Cylinders," SRI Final Report, Contract N00178-74-C-0450, Naval Surface Weapons Center, Dahlgren, Virginia (August 1975).
3. L. Seaman, "TROT Computer Code for Two-Dimensional Stress Wave Propagation," SRI Final Report, Volume III, Contract No. DAAK11-77-C-0083, U.S. Army Ballistic Research Laboratories, Aberdeen Proving Ground, Maryland (August 1978).
4. L. Seaman, "SRI PUFF 8 Computer Program for One-Dimensional Stress Wave Propagation," SRI Final Report, Volume II, Contract No. DAAK11-77-C-0083, U.S. Army Ballistic Research Laboratories, Aberdeen Proving Ground, Maryland (August 1978).
5. H. C. Hornig, E. L. Lee, M. Finger, and J. E. Kurrle, "Equation of State of Detonation Products," ONR Report DR-163, presented at the Fifth Symposium on Detonation (August 1970).
6. T. W. Burkee, Jr., L. Seaman, R. Crewdson, and D. Curran, "Dynamic Fracture Criteria for Ductile and Brittle Metals," J. of Materials, 7 (3), 393-401. (1972).
7. N. G. Chetayev, The Stability of Motion, translated from the Russian by M. Nadler. (Pergamon Press, 1961).
8. R. Hill, J. Mech. Phys. Solids, 10, 1 (1962).
9. J. W. Rudnicki and J. R. Rice, "Conditions for the Localization of Deformation in Pressure-Sensitive Dilatant Materials," J. Mech. Phys. Solids, 23, 371-394 (1975).
10. R. J. Asaro and J. R. Rice, "Strain Localization in Ductile Single Crystals," J. Mech. Phys. Solids, 25, 309-338 (1977).
11. J. R. Rice, "The Localization of Plastic Deformation," in Theoretical and Applied Mechanics, W. T. Koiter, ed. (North-Holland Publishing, 1976).

12. R. M. Davies, "Stress Waves in Solids," in Surveys in Mechanics, C. K. Batchelor and R. M. Davies, eds. (Cambridge, 1956).
13. O. E. Jones, F. W. Neilson, and W. B. Benedick, J. Appl. Phys. 33, (11) 3224-3232 (November 1962).
14. D. C. Erlich, L. Seaman, and D. R. Curran, "A Preliminary Study of Armor Penetration by Shear Banding," SRI Final Report, Volume 1, Contract No. DAAK11-77-G0083, for U.S. Army Ballistics Research Laboratory, Aberdeen Proving Ground, Maryland (August 1978).
15. A. L. Wingrove, "The Influence of Projectile Geometry on Adiabatic Shear and Target Failure," Mat. Trans, 4, 1829 (1973).
16. V. S. Lindholm and C. R. Hargreaves, "Dynamic Testing of High Strength Steels and their Susceptibility to Inhomogeneous Shear," Proceedings of the 2nd Internat. Conf. of Mech. Behavior of Mater. (August 1976).
17. J. C. Lemain and W. A. Backofen, "Adiabatic Instability in the Orthogonal Cutting of Steel," Metallurgical Transactions, 3, (February 1972).
18. D. A. Shockey, Private communication.

DISTRIBUTION LIST

No. of Copies	To
1	Office of the Under Secretary of Defense for Research and Engineering, The Pentagon, Washington, D.C. 20301
12	Commander, Defense Technical Information Center, Cameron Station, Building 5, 5010 Duke Street, Alexandria, Virginia 22314
1	Metals and Ceramics Information Center, Battelle Columbus Laboratories, 505 Kinn Avenue, Columbus, Ohio 43201
1	Deputy Chief of Staff, Research, Development, and Acquisition, Headquarters Department of the Army, Washington, D. C. 20310
1	ATTN: DAMA-ARZ
1	Dr. J. Bryant
1	Commander, Army Research Office, P. O. Box 12211, Research Triangle Park, North Carolina 27709
1	ATTN: Information Processing Office
1	Dr. E. Saibel
1	Dr. G. Mayer
1	Dr. F. Dressel
1	Dr. F. W. Schmiedeshoff
1	Commander, U. S. Army Materiel Development and Readiness Command, 5001 Eisenhower Avenue, Alexandria, Virginia 22333
1	ATTN: DRCLM
1	Commander, U. S. Army Materiel Systems Analysis Activity, Aberdeen Proving Ground, Maryland 21005
1	ATTN: DRXSY-MP, H. Cohen
1	Commander, U. S. Army Electronics Research and Development Command, Fort Monmouth, New Jersey 07703
1	ATTN: DELSD-L
1	DELSO-E
1	Commander, U. S. Army Missile Command, Redstone Arsenal, Alabama 35899
1	ATTN: DRSMI-RKP, J. Wright, Bldg. 7544
1	Technical Library
1	DRSMI-TB, Redstone Scientific Information Center
1	Commander, U. S. Army Natick Research and Development Command, Natick, Massachusetts 01760
1	ATTN: Technical Library
1	Dr. E. W. Ross
1	DRDNA-UE, Dr. L. A. McClaine
1	Mr. J. Flanagan
1	Commander, U. S. Army Tank-Automotive Research and Development Command, Warren, Michigan 48090
1	ATTN: DRDTA-UL, Technical Library
1	Mr. V. Pagano
1	Commander, U. S. Army Armament Research and Development Command, Dover, New Jersey 07801
1	ATTN: Technical Library
1	DRDAP-SCM, J. D. Corrie
1	Dr. J. Brinkman
1	Dr. J. Miller
1	Mr. J. Reetle
1	Dr. J. Fraiser
1	Mr. Harry E. Peibly, Jr., PLASTEC, Director
1	Mr. T. Knight
1	Mr. J. Herschkowitz
1	Mr. B. Konrad
1	Mr. W. Pryor
1	Mr. J. Pearson
1	G. Randers-Pehrson
1	Mr. A. Garcia
1	Commander, Rock Island Arsenal, Rock Island, Illinois 61299
1	ATTN: Mr. R. Nelson

No. of Copies	To
1	Director, U. S. Army Ballistic Research Laboratory, Aberdeen Proving Ground, Maryland 21005
1	ATTN: Dr. A. Dietrich
1	Dr. J. Suckling
1	Dr. J. Zukas
1	Dr. R. Vitali
1	Dr. G. L. Filbey
1	Dr. W. Gillich
1	Dr. G. Moss
1	ORDAR-TSB-S (STINFO)
1	Commander, Harry Diamond Laboratories, 2800 Powder Mill Road, Adelphi, Maryland 20783
1	ATTN: Technical Information Office
1	Commander, Watervliet Arsenal, Watervliet, New York 12189
1	ATTN: Dr. T. Davidson
1	Mr. D. P. Kendall
1	Mr. J. F. Throck
1	Commander, U. S. Army Foreign Science and Technology Center, 220 7th Street, N. E., Charlottesville, Virginia 22901
1	ATTN: Mr. Marley, Military Tech
1	Chief, Benet Weapons Laboratory, LCWSL, USA ARRADCOM, Watervliet Arsenal, Watervliet, New York 12189
1	ATTN: DRDAR-LCB-TL
1	Director, Eustis Directorate, U. S. Army Air Mobility Research and Development Laboratory, Fort Eustis, Virginia 23604
1	ATTN: Mr. J. Robinson, DAVDL-E-MOS (AVRADCOM)
1	Commander, USACDC Air Defense Agency, Fort Bliss, Texas 79916
1	ATTN: Technical Library
1	Commander, U. S. Army Engineer School, Fort Belvoir, Virginia 22060
1	ATTN: Library
1	Commander, U. S. Army Engineer Waterways Experiment Station, Vicksburg, Mississippi 39180
1	ATTN: Research Center Library
1	Commander, U. S. Army Mobility Equipment Research and Development Center, Fort Belvoir, Virginia 22060
1	ATTN: Mr. William H. Baer, Materials Research Laboratory
1	Director, Structural Mechanics Research, Office of Naval Research, 800 North Quincy Street, Arlington, Virginia 22203
1	ATTN: Dr. N. Perrone
1	Naval Research Laboratory, Washington, D.C. 20375
1	ATTN: C. D. Beachem, Head, Adv. Mat'l's Tech Br. (Code 6310)
1	Dr. J. M. Krafft - Code 8430
1	Dr. P. P. Puzak
1	Dr. Jim C. I. Chang
1	Naval Ship Research and Development Laboratory, Annapolis, Maryland 21402
1	ATTN: Dr. H. P. Chu
1	Chief of Naval Research, Arlington, Virginia 22217
1	ATTN: Code 471
1	Naval Surface Weapons Center, Dahlgren, Virginia 22448
1	ATTN: W. Mannschreck
1	W. Mock
1	D. Brunson
1	Mr. W. H. Holt
1	Technical Library

No. of Copies	To	
1	Naval Surface Weapons Center, Silver Spring, Maryland	20910
1	ATTN: Dr. R. Crowe	
1	Technical Library	
1	Naval Weapons Laboratory, Washington, D.C.	20390
1	ATTN: H. W. Pomine, Mail Stop 103	
1	Naval Weapons Center, China Lake, California	93555
1	ATTN: Mr. M. Backman	
1	Dr. J. Pearson	
2	Air Force Materials Laboratory, Wright-Patterson Air Force Base, Ohio	45433
1	ATTN: AFML (MXE), E. Morrissey	
1	AFML (LC)	
1	AFML (LLP), D. M. Forney, Jr.	
1	AFML (LNC), T. J. Reinhart	
1	AFML (MBC), Mr. Stanley Schulman	
1	AFMFL (FB), Dr. J. C. Halpin	
1	Dr. T. Nicholas	
1	Air Force Flight Dynamics Laboratory, Wright-Patterson Air Force Base, Ohio	45433
1	ATTN: AFMFL (FBS), C. Wallace	
1	Library	
1	National Aeronautics and Space Administration, Washington, D.C.	20546
1	ATTN: Mr. B. G. Achhammer	
1	Mr. G. C. Deutsch - Code RW	
1	National Aeronautics and Space Administration, Marshall Space Flight Center, Huntsville, Alabama	35812
1	ATTN: R. J. Schwinghamer, EH01, Dir., M&P Lab	
1	Mr. W. A. Wilson, EH41, Bldg. 4612	
1	National Bureau of Standards, U. S. Department of Commerce, Washington, D.C.	21234
1	ATTN: Mr. J. A. Bennett	
1	Mechanical Properties Data Center, Belfour Stulen Inc., 13917 W. Ray Shore Drive, Traverse City, Michigan	49684
1	Honeywell, Inc., Research Dept., SBRC, Mail Stop A3 340, 2345 Walnut Street, Saint Paul, Minnesota	55113
1	ATTN: Mr. Gene Fisher	
1	Dr. Gordon Johnson	
1	Prof. I. Fyfe, University of Washington, Department of Aeronautics and Astronautics, Seattle, Washington	98105
1	Stanford Research Institute, Menlo Park, California	94025
1	ATTN: Dr. D. Curran	
1	Dr. L. Seaman	
1	Dr. D. Shockey	
1	Dr. G. Abrahamson	
1	Dr. D. Erlich	
1	Dr. R. Caligiuri	
1	Systems, Science and Software, P. O. Box 1620, La Jolla, California	92037
1	ATTN: Dr. R. Sedgwick	
1	Sandia Corporation, Kirkland East, Albuquerque, New Mexico	87115
1	ATTN: Dr. B. Rutherford	
1	Dr. A. Stevens	
1	Dr. W. Herrmann	
1	Dr. L. Bartholf	
1	Dr. S. Benzley	
1	Southwest Research Institute, 8500 Culebra Road, San Antonio, Texas	78284
1	ATTN: Prof. H. Lindholm	
1	Dr. W. Baker	
1	Dr. George P. Irwin, Department of Mechanical Engineering, University of Maryland, College Park, Maryland	20742

No. of Copies	To	
1	Battelle Columbus Laboratories, 505 King Avenue, Columbus, Ohio	43201
1	ATTN: E. Hulbert	
1	Brown University, Providence, Rhode Island	02912
1	ATTN: Prof. J. R. Rice	
1	Prof. W. N. Findley, Division of Engineering, Box D	
1	Prof. R. Clifton	
1	Prof. J. Duffey	
1	Carnegie-Mellon University, Department of Mechanical Engineering, Schenley Park, Pittsburgh, Pennsylvania	15213
1	ATTN: Dr. J. L. Swedlow	
1	Prof. J. D. Lubahn, Colorado School of Mines, Golden, Colorado	80401
1	Prof. J. Dvorak, Civil Engineering Department, University of Utah, Salt Lake City, Utah	84112
1	George Washington University, School of Engineering and Applied Sciences, Washington, D.C.	20052
1	ATTN: Dr. H. Liebowitz	
1	Terra Tek, University Research Park, 420 Wakara Way, Salt Lake City, Utah	84108
1	ATTN: Mr. S. Green	
1	Dr. A. Jones	
1	Drexel University, Department of Materials Science, Market and Chestnut Streets, Philadelphia, Pennsylvania	19104
1	ATTN: Prof. H. C. Rogers	
1	Washington State University, Department of Physics, Pullman, Washington	99163
1	ATTN: Prof. G. Duvall	
1	Prof. R. Fowles	
1	Massachusetts Institute of Technology, Cambridge, Massachusetts	02139
1	ATTN: Prof. F. A. McClintock, Room 1-304	
1	Prof. R. M. Pelloux	
1	Prof. T. H. H. Pian, Department of Aeronautics and Astronautics	
1	Prof. A. S. Argon, Room 1-306	
1	Dr. Gregory Olson, Dept. of Metallurgy	
1	Dr. D. Parks, Dept. of Mech. Eng.	
1	Syracuse University, Department of Chemical Engineering and Metallurgy, 409 Link Hall, Syracuse, New York	13210
1	ATTN: Dr. V. Weiss, Metallurgical Research Labs., Bldg. D-6	
1	Prof. W. Goldsmith, Department of Mechanical Engineering, University of California, Berkeley, California	94720
1	University of California, Los Alamos Scientific Laboratory, Los Alamos, New Mexico	87544
1	ATTN: Dr. R. Karop	
1	Dr. J. M. Walsh	
1	Technical Library	
1	Prof. A. J. McEvily, Metallurgy Department U-136, University of Connecticut, Storrs, Connecticut	06268
1	Prof. D. Drucker, Dean of School of Engineering, University of Illinois, Champaign, Illinois	61820
1	University of Illinois, Urbana, Illinois	61801
1	ATTN: Prof. T. J. Dolan, Department of Theoretical and Applied Mechanics	
1	Prof. T. Landman, Dept. of Theoretical and Applied Mechanics	
1	Dr. M. L. Williams, Dean of Engineering, 240 Benedum Hall, University of Pittsburgh, Pittsburgh, Pennsylvania	15260
1	Prof. A. Kobayashi, Department of Mechanical Engineering, FU-10, University of Washington, Seattle, Washington	98195

No. of Copies	To
1	R. Sedgwick, Systems Science Software, La Jolla, California 92037
1	Prof. W. F. Riley, Dept. of Eng. Mech., Iowa State University, Ames, Iowa 50010
1	Prof. I. Fyfe, Dept. of Aero. Eng., University of Washington, Seattle, Washington 98105
	State University of New York at Stony Brook, Stony Brook, New York 11790
1	ATTN: Prof. Fu-Pen Chiang, Department of Mechanics
	Lawrence Livermore Laboratory, Livermore, California 94550
1	ATTN: Dr. R. Toland
1	Dr. M. Wilkins
1	Dr. M. Guinan

No. of Copies	To
	Denver Research Institute, 2390 South University Boulevard, Denver, Colorado 80210
1	ATTN: Dr. K. Recht
1	Dr. C. Hoggart
	Director, Army Materials and Mechanics Research Center, Watertown, Massachusetts 02172
2	ATTN: DRXMR-PL
1	DRXMR-PR
1	DRXMR-PD
1	DRXMR-AP
26	DRXMR-TE, Mr. J. Mescall

AD

Army Materials and Mechanics Research Center,
Watertown, Massachusetts 02172
FURTHER DEVELOPMENT OF A
COMPUTATIONAL SHEAR BAND MODEL
D. C. Erlich, D. R. Curran, and L. Seaman,
SRI, International, Menlo Park, Calif. 94025
Technical Report AMMRC TR 80-3, March 1980,
84 pp -illus - tables,
Contract DAAG46-77-C-0043
Final Report, May 1977 - September 1978

UNCLASSIFIED
UNLIMITED DISTRIBUTION

Key Words
Shear banding
Fragmenting rounds
Material properties
Dynamic experiments
Constitutive relations
Wave propagation

Experimental and analytical work was performed to improve the previously developed SRI computational model for adiabatic shear band nucleation and growth (SNAG). A series of "contained" fragmenting cylinder experiments were performed with 4340 steel treated to hardness of R_c40 , R_c52 , and R_c21 . The resulting damage ranged from homogeneous plastic deformation to extensive shear banding and resulting fragmentation. The results showed strong positive correlation between shear banding damage and material hardness for identical loading conditions. A simplified method of damage quantification was used to obtain shear band density, size and orientation distributions for all of the R_c40 experiments.

AD

Army Materials and Mechanics Research Center,
Watertown, Massachusetts 02172
FURTHER DEVELOPMENT OF A
COMPUTATIONAL SHEAR BAND MODEL
D. C. Erlich, D. R. Curran, and L. Seaman,
SRI, International, Menlo Park, Calif. 94025
Technical Report AMMRC TR 80-3, March 1980,
84 pp -illus - tables,
Contract DAAG46-77-C-0043
Final Report, May 1977 - September 1978

UNCLASSIFIED
UNLIMITED DISTRIBUTION

Key Words
Shear banding
Fragmenting rounds
Material properties
Dynamic experiments
Constitutive relations
Wave propagation

Experimental and analytical work was performed to improve the previously developed SRI computational model for adiabatic shear band nucleation and growth (SNAG). A series of "contained" fragmenting cylinder experiments were performed with 4340 steel treated to hardness of R_c40 , R_c52 , and R_c21 . The resulting damage ranged from homogeneous plastic deformation to extensive shear banding and resulting fragmentation. The results showed strong positive correlation between shear banding damage and material hardness for identical loading conditions. A simplified method of damage quantification was used to obtain shear band density, size and orientation distributions for all of the R_c40 experiments.

AD

Army Materials and Mechanics Research Center,
Watertown, Massachusetts 02172
FURTHER DEVELOPMENT OF A
COMPUTATIONAL SHEAR BAND MODEL
D. C. Erlich, D. R. Curran, and L. Seaman,
SRI, International, Menlo Park, Calif. 94025
Technical Report AMMRC TR 80-3, March 1980,
84 pp -illus - tables,
Contract DAAG46-77-C-0043
Final Report, May 1977 - September 1978

UNCLASSIFIED
UNLIMITED DISTRIBUTION

Key Words
Shear banding
Fragmenting rounds
Material properties
Dynamic experiments
Constitutive relations
Wave propagation

Experimental and analytical work was performed to improve the previously developed SRI computational model for adiabatic shear band nucleation and growth (SNAG). A series of "contained" fragmenting cylinder experiments were performed with 4340 steel treated to hardness of R_c40 , R_c52 , and R_c21 . The resulting damage ranged from homogeneous plastic deformation to extensive shear banding and resulting fragmentation. The results showed strong positive correlation between shear banding damage and material hardness for identical loading conditions. A simplified method of damage quantification was used to obtain shear band density, size and orientation distributions for all of the R_c40 experiments.

AD

Army Materials and Mechanics Research Center,
Watertown, Massachusetts 02172
FURTHER DEVELOPMENT OF A
COMPUTATIONAL SHEAR BAND MODEL
D. C. Erlich, D. R. Curran, and L. Seaman,
SRI, International, Menlo Park, Calif. 94025
Technical Report AMMRC TR 80-3, March 1980,
84 pp -illus - tables,
Contract DAAG46-77-C-0043
Final Report, May 1977 - September 1978

UNCLASSIFIED
UNLIMITED DISTRIBUTION

Key Words
Shear banding
Fragmenting rounds
Material properties
Dynamic experiments
Constitutive relations
Wave propagation

Experimental and analytical work was performed to improve the previously developed SRI computational model for adiabatic shear band nucleation and growth (SNAG). A series of "contained" fragmenting cylinder experiments were performed with 4340 steel treated to hardness of R_c40 , R_c52 , and R_c21 . The resulting damage ranged from homogeneous plastic deformation to extensive shear banding and resulting fragmentation. The results showed strong positive correlation between shear banding damage and material hardness for identical loading conditions. A simplified method of damage quantification was used to obtain shear band density, size and orientation distributions for all of the R_c40 experiments.

Preliminary computer simulations were performed to determine plastic shear strain rate histories in the direction of the predominant shear banding orientation mode, and the computations were compared with experimental data to yield first estimates for the values of the nucleation and growth parameters.

A shear band nucleation criterion based on measurable material properties was proposed and tested against the experimental data; the criterion was seen to be promising although not yet conclusive.

Several experimental techniques for characterizing the shear banding resistance of materials were evaluated and compared. The contained fragmenting cylinder experiment was concluded to be the best single technique, although the dynamic punch test has special value for armor penetration applications.

Preliminary computer simulations were performed to determine plastic shear strain rate histories in the direction of the predominant shear banding orientation mode, and the computations were compared with experimental data to yield first estimates for the values of the nucleation and growth parameters.

A shear band nucleation criterion based on measurable material properties was proposed and tested against the experimental data; the criterion was seen to be promising although not yet conclusive.

Several experimental techniques for characterizing the shear banding resistance of materials were evaluated and compared. The contained fragmenting cylinder experiment was concluded to be the best single technique, although the dynamic punch test has special value for armor penetration applications.

Preliminary computer simulations were performed to determine plastic shear strain rate histories in the direction of the predominant shear banding orientation mode, and the computations were compared with experimental data to yield first estimates for the values of the nucleation and growth parameters.

A shear band nucleation criterion based on measurable material properties was proposed and tested against the experimental data; the criterion was seen to be promising although not yet conclusive.

Several experimental techniques for characterizing the shear banding resistance of materials were evaluated and compared. The contained fragmenting cylinder experiment was concluded to be the best single technique, although the dynamic punch test has special value for armor penetration applications.

Preliminary computer simulations were performed to determine plastic shear strain rate histories in the direction of the predominant shear banding orientation mode, and the computations were compared with experimental data to yield first estimates for the values of the nucleation and growth parameters.

A shear band nucleation criterion based on measurable material properties was proposed and tested against the experimental data; the criterion was seen to be promising although not yet conclusive.

Several experimental techniques for characterizing the shear banding resistance of materials were evaluated and compared. The contained fragmenting cylinder experiment was concluded to be the best single technique, although the dynamic punch test has special value for armor penetration applications.